# Multiscale modelling of wall-to-bed heat transfer in fixed beds with non-spherical pellets From particle-resolved CFD to pseudo-homogenous models

Moghaddam, E. M.; Foumeny, Esmail A.; Stankiewicz, A. I.; Padding, J. T.

**DOI**
10.1016/j.ces.2021.116532

**Publication date**
2021

**Document Version**
Final published version

**Published in**
Chemical Engineering Science

Chemical Engineering Science 236 (2021) 116532

Contents lists available at ScienceDirect

Chemical Engineering Science

journal homepage: www.elsevier.com/locate/ces

# Multiscale modelling of wall-to-bed heat transfer in fixed beds with non-spherical pellets: From particle-resolved CFD to pseudo-homogenous models

E.M. Moghaddam, E.A. Foumeny, A.I. Stankiewicz, J.T. Padding *

*Process & Energy Department, Delft University of Technology, the Netherlands*

## HIGHLIGHTS

- Study of forced convection heat transfer through packed beds.
- Discrete pellet effects in narrow tubes with spheres, cylinders and Raschig rings.
- Significant local deviations from pseudo-homogenous model predictions.
- Exposition of length-dependence of effective heat transfer parameters.

## GRAPHICAL ABSTRACT

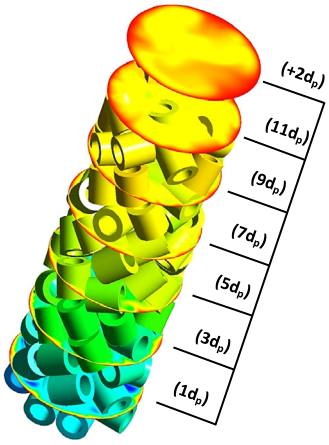


## ARTICLE INFO

*Article history:*
Received 25 September 2020
Received in revised form 10 February 2021
Accepted 12 February 2021
Available online 19 February 2021

*Keywords:*
Rigid Body Dynamics
Particle-resolved CFD Simulations
Packing
Raschig rings
Effective heat transfer parameters
Length dependency

## ABSTRACT

We investigate forced convective heat transfer in packings of spheres, cylinders and Raschig rings, made of glass, steel and alumina, in relatively narrow tubes. A detailed comparison is made between resolved pellet-scale, azimuthally-averaged temperature profiles, and 2D-axially-dispersed pseudo-homogenous plug flow (2D-ADPF) predictions. The local temperature deviates significantly from azimuthally-averaged profiles, which in turn deviate from 2D-ADPF predictions. We show that the length dependency of effective heat transfer parameters is caused by thermal (non-)equilibrium between fluid and solid phases along the bed and not related to inadequate insulation of the calming section or the thermocouple's cross or an under-developed velocity and thermal field at the bed inlet. The influence of pellet shape and thermal conductivity and tube-to-pellet diameter ratio on $k_{er}$ and $h_w$ are assessed. We conclude that the models of Specchia/Baldi/Gianetto/Sicardi for all flow regimes and of Martin/Nilles for the turbulent regime are recommended for practical use for spherical particles.



## 1. Introduction

Prediction of wall-to-bed heat transfer rate in fixed bed reactors is a topic of continuing interest in reactor design (Dixon and Dongeren, 1998; Dong et al., 2017; Eppinger et al., 2011; Jurtz

* Corresponding author.
*E-mail address:* j.t.padding@tudelft.nl (J.T. Padding).

https://doi.org/10.1016/j.ces.2021.116532
0009-2509/

**Nomenclature**

| | |
|---|---|
| $Bi$ | Apparent wall Biot number; $Bi = h_w R_t/k_{er}$ [–] |
| $c_p$ | Fluid heat capacity [J $kg^{-1}$ $K^{-1}$] |
| $d_p$ | Diameter of sphere or cylinder [m] |
| $d_{po}$ | Outer diameter of ring [m] |
| $d_{pi}$ | Inner diameter of ring [m] |
| $d_{pv}$ | Diameter of a sphere of equal volume [m] |
| $d_t$ | Tube or bed diameter [m] |
| G | Mass flux [kg $m^{-2}$ $s^{-1}$] |
| $h_p$ | Height of cylinder or ring [m] |
| $h_w$ | Apparent wall heat transfer coefficient [$Wm^{-2}K^{-1}$] |
| I | Turbulence intensity [–] |
| $k_{af}$ | Effective (axial) fluid phase thermal conductivity [$Wm^{-1}K^{-1}$] |
| $k_{as}$ | Effective (axial) solid phase thermal conductivity [$Wm^{-1}K^{-1}$] |
| $k_{ea}$ | Effective axial thermal conductivity [$Wm^{-1}K^{-1}$] |
| $k_{er}$ | Effective radial thermal conductivity [$Wm^{-1}K^{-1}$] |
| $k_f$ | Fluid thermal conductivity [$Wm^{-1}K^{-1}$] |
| $k_p$ | Pellet (solid) thermal conductivity [$Wm^{-1}K^{-1}$] |
| L | Bed length [m] |
| n | Number of CFD cell faces (at certain cross section) [–] |
| N | Tube-to-pellet diameter ratio [–] |
| $N_{pv}$ | Tube-to-pellet diameter ratio based on $d_{pv}$ [–] |
| $Nu_w$ | Apparent wall Nusselt number; $Nu_w = h_w d_{pv}/k_f$ [–] |
| $Pe_{ea}$ | Effective axial Peclet numbers; $Pe_{ea} = Gc_p d_{pv}/k_{ea}$ [–] |
| $Pe_{er}$ | Effective radial Peclet numbers; $Pe_{er} = Gc_p d_{pv}/k_{er}$ [–] |
| $Pr$ | Prandtl number; $Pr = \mu c_p/k_f$ [–] |
| $q_w$ | Wall heat flux [$Wm^{-2}$] |
| r | Radial coordinate [m] |
| $R_t$ | Bed radius; $R_t = d_t/2$ [m] |
| $Re_p$ | Reynolds number based on $d_{pv}$; $Re_p = \rho v_0 d_{pv}/\mu$ [–] |
| T | Temperature [K] |
| $T_{CFD}$ | Temperature measured in CFD simulation [K] |
| $T_{pre}$ | Temperature predicted by 2D-ADPF model [K] |
| $T_w$ | Wall temperature [K] |
| $T_0$ | Inlet fluid temperature [K] |
| $v_z$ | Azimuthally-averaged axial velocity [m $s^{-1}$] |
| z | Axial coordinate [m] |

*Greek Letters*

| | |
|---|---|
| $\varepsilon$ | Bulk porosity [–] |
| $\zeta$ | Axial dimensionless coordinate; $\zeta = z/R_t$ [–] |
| $\omega$ | Radial dimensionless coordinate; $\omega = r/R_t$ [–] |
| $\theta$ | Dimensionless temperature; $\theta = (T_w - T)/(T_w - T_0)$ [–] |
| $\mu$ | Fluid dynamic viscosity [kg $m^{-1}$ $s^{-1}$] |
| $\rho$ | Fluid phase density [kg $m^{-3}$] |

et al., 2019; Moghaddam et al., 2019; Paterson and Carberry, 1983; Romkes et al., 2003; Taskin et al., 2008). Of particular concern is the case of tubular fixed bed reactors with low tube-to-pellet diameter ratio ($N$) due to their inherent advantage of enhanced wall-to-bed heat transport, which is essential for handling highly exothermic and endothermic reactions. Many researchers use classical pseudo-homogenous $k_{er}$-$h_w$ models, using an effective radial thermal conductivity $k_{er}$ and an apparent wall heat transfer coefficient $h_w$ (see e.g. Bey and Eigenberger, 2001; Borkink and Westerterp, 1992; Dai et al., 2014; Dixon, 1996; Nekhamkina and Sheintuch, 2009; Obalová et al., 2012; Schlereth and Hinrichsen, 2014), which provide continuous radial and axial temperature profiles. Such 2D models assume that the rate of thermal transport across the catalyst bed can be described effectively by single homogenous phase transport rather than distinct solid and gas phase events (Dixon, 2012; Paterson and Carberry, 1983). Homogeneous models are often preferred for fast design, optimization and control of fixed bed reactors. Nonetheless, current research based on 3D particle-resolved Computational Fluid Dynamics (CFD) simulations shows a substantial influence of local structure on both the velocity and temperature fields, particularly in low-$N$ tubular fixed beds (Behnam et al., 2013; Dong et al., 2017; Eppinger et al., 2011; Jurtz et al., 2019; Magnico, 2009; Moghaddam et al., 2019, 2020, 2021). For example, several research groups, e.g. Dong et al., (2017), Freund et al. (2003), Magnico, (2009), Moghaddam et al. (2019,2020,2021), Flaischlen and Wehinger (2019), demonstrated that 2D pseudo-homogenous models are not sufficient to precisely describe the sharp temperature and composition profiles occurring in narrow-tube fixed bed reactors. The inadequacy mainly arises because: i) the condition of spatial homogeneity of structures cannot be fulfilled in low-$N$ packed bed reactors, ii) the premise of plug flow in such models conceals the important role of flow maldistribution on the local transport processes (Dong et al., 2017; Jurtz et al., 2019; Moghaddam et al., 2019), iii) these models rely strongly on effective transport parameters which are given in the form of empirical correlations and calculated by solving an inverse problem such that the best fit with experimental data is obtained. As shown by Vortmeyer and Haidegger (1991) and Wen and Ding (2006), there is a large disagreement between the predicted values and literature correlations for the effective radial Peclet number, $Pe_{er} = Gc_p d_{pv}/k_{er}$, and the apparent wall Nusselt number, $Nu_w = h_w d_{pv}/k_f$, versus particle Reynolds number, $Re_p$ (see Nomenclature for clarification of the meaning of symbols). Furthermore, these empirical correlations thoroughly reflect the impact of catalyst shape, tube-to-pellet diameter ratio and operating conditions and, thus, are not recommended for extrapolation (Magnico, 2009; Nijemeisland and Dixon, 2001). Besides, several research groups have noticed that using a 2D-plug flow (2D-PF) heat transfer model as the fitting model, both $k_{er}$ and $h_w$ evaluated from the temperature profiles show a bed length dependency (Wen and Ding (2006); Dixon, 2012, 1985; Freiwald and Paterson, 1992). Paterson and Carberry (1983) demonstrated that the disagreement between observed and computed hot spots may be attributed to either neglecting the axial heat dispersion term in the model or to the use of length-dependent parameters in the heat transfer models. In fact, the authors suggested the use of a 2D-axially-dispersed pseudo-homogenous plug flow (2D-ADPF) model, which includes axial dispersion terms, to overcome the length dependency problem. Earlier researches, e.g. by Gunn and Khalid (1975) and Dixon et al. (1978), have shown that when the 2D-ADPF model with three parameters, i.e. $k_{ea}$, $k_{er}$ and $h_w$, is fitted to the thermal data for different bed lengths, results do not reveal any length dependency. However, the values of $k_{ea}$ were poorly overestimated, being larger than the realistic values by an order of magnitude. This observation has resulted in a debate about the use of $k_{ea}$ as one of the three fitted parameters in the 2D-ADPF model (Li and Finlyson, 1976; Paterson and Carberry, 1983).

Following these studies, Dixon (1985) investigated the influence of bed length on the effective parameters using several heat transfer experiments. The author observed that $k_{er}$ and $h_w$ decrease to asymptotic values along the bed depth even when the 2D-ADPF

model with a fixed predefined $k_{ea}$ is used as a fitting model. Moreover, he explained that the heat conduction along the length of the tube wall from the heated test section to the unheated calming section leads to preheating of the inlet gas (see Fig. 1) and, therefore, a radially varying temperature profile at the bed inlet instead of a constant temperature, thereby leading to the so-called "length effect" in $k_{er}$ and $h_w$. Similar conclusions were also reached by Freiwald and Paterson (1992) and Borkink and Westerterp (1992). They found that the length dependence effect could be eliminated by using the 2D-ADPF model instead of the 2D-PF model, provided that the heat loss from the calming section and thermocouple cross are either effectively avoided or taken into account in the modelling by improving the inlet temperature boundary condition.

Overall, with a multiplicity of still unsettled ambiguities concerned with the limitations of pseudo-homogenous models, i.e. 2D-(AD)PF models, one may presume that the reported discrepancies with experimental observations (Dixon et al., 2006; Nijemeisland and Dixon, 2001; Wen and Ding, 2006) can be ascribed to shortcomings in the rate equations which treat a two-phase tortuous medium as 2D-interpenetrating continua or a 2D-quasi-homogenous system.

In the last two decades, researchers have used CFD simulations to address the local physiochemical phenomena in fixed bed reactors (Partopour and Dixon, 2019). This approach is based on spatially resolved simulations, which enable capturing many important local flow features and transport properties at pellet-scale in tubular fixed bed reactors (Bale et al., 2017, 2018; Dixon et al., 2012; Dong et al., 2017; Eppinger et al., 2011; Freund et al., 2003, 2005; Guo et al., 2019; Moghaddam et al., 2019; Singhal et al., 2017a; Wehinger et al., 2017). In the last decade, such particle-resolved CFD simulations have improved by using advanced algorithms to synthesize 3D packing surrogates with different particle shapes. Packing algorithms include Discrete Element Methods (DEM) (Dong et al., 2017; Flaischlen and Wehinger, 2019; Guo et al., 2019; Ruiz et al., 2019; Singhal et al., 2017b), Monte-Carlo methods (Behnam et al., 2013) and Rigid Body Dynamics (RBD) tools such as the open-source graphical software Blender (Boccardo et al., 2015; Partopour and Dixon, 2017) or in-house RBD codes (Moghaddam et al., 2019).

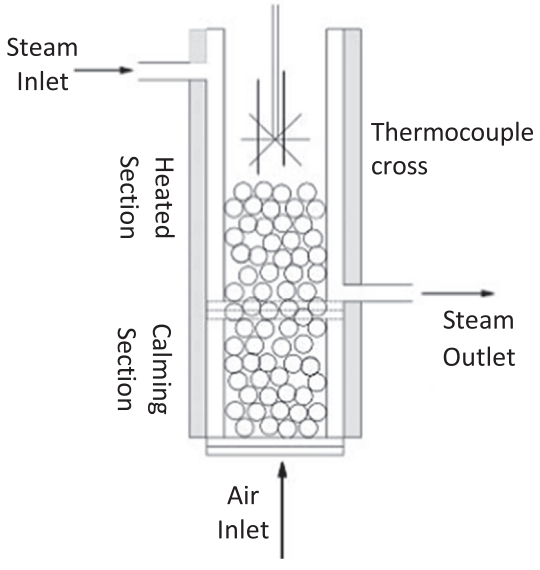


**Fig. 1.** Schematic drawing of a generic laboratory heat transfer experiment for steam heating of a flowing gas through a bed of particles. The fluid is passed through an unheated packing calming section to establish a velocity profile, and then flows into the heated section. In this example a thermocouple cross is positioned above the packing to measure radial temperature profiles (after Dixon, 2012).

In this study, we will use the RBD-CFD approach, elaborated and validated in our previous works Moghaddam et al. (2019, 2020, 2021), to investigate the prevailing ambiguities associated with the classical 2D-pseudohomogenous $k_{er}$-$h_w$ model, i.e. the 2D-ADPF heat transfer model, focusing in particular on the problem of the length dependency of the effective heat transfer parameters. To this end, we will consider a wall-heated fixed bed heat transfer problem in packed tubes with spheres, equilateral cylinders and Raschig rings for a wide range of $Re_p$ with $N$ in the range of 3–6. Furthermore, we will elucidate different features of the radial temperature profile obtained from 2D-ADPF heat transfer model by comparing it to the azimuthally averaged 3D temperature fields predicted by 3D discrete-pellet CFD simulations.

## 2. 3D discrete-pellet CFD modelling

Since this study is a follow-up of our previous research (Moghaddam et al., 2018, 2019, 2020, 2021), in which the framework of sequential RBD-CFD modelling is elaborated, here we only briefly address the setup procedures for RBD and CFD simulations.

### 2.1. Generating 3D particle packing structures

Random packings of spheres, equilateral cylinders and Raschig rings are synthesised using our RBD-based packing algorithm (Moghaddam et al., 2018). The RBD-algorithm is based on a hard body approach for handling collision phenomena and uses a cut-off on the relative contact velocities to control the transition between moving and resting particles, thereby stabilizing the convergence in packing simulations.

For the simulations described here, a reactor tube is represented by a simple open-top empty cylinder with a height of 150 mm and different diameters (see Table 1), constructed by triangular face meshes. A preset number of particles, i.e. spheres, cylinders or Raschig rings, is then placed in a vertical column above the vertical tube, where cylinders and Raschig rings are placed obliquely with an angle of 45° between their symmetry axis and the vertical direction, and fall freely under the influence of a gravitational field to the bottom of the tube (see Moghaddam et al., 2018, for more details). A force-torque balance, together with other auxiliary models accounting for interactions between pellets and between pellets and tube wall, i.e. collisional contacts and resting contacts, is solved over a time span to simulate the pellet loading process. The particle packing simulation stops when a dynamic equilibrium based on the work-energy theory is attained. Since the resulting mean and local porosities of the RBD-simulated structures are strongly affected by the physio-mechanical properties of pellets and container, tube-to-pellet diameter ratio and the loading method, we followed the validated procedure presented in our previous study (Moghaddam et al., 2018) to synthesize the densest possible random packings of spheres, cylinders and Raschig rings. Details of the pellet properties and settings used in the RBD simulations are presented in Table 1. Furthermore, a detailed validation study and sensitivity analysis concerning the influence of loading methods and pellet properties on the particle packing process and the resulted packing structures has been presented in the original paper.

Typical computer-generated random packings of spheres, cylinders and Raschig rings with $N_{pv}$ (tube-to-pellet diameter ratio based on the sphere diameter of equivalent pellet volume) approximately equal to 4 are shown in Fig. 2.

**Table 1**
Pellet properties and settings used in RBD simulations for packing generation.

| Case studies and parameters | Setup value | |
|---|---|---|
| Spheres | Pellet size [mm] | $d_p$:10 |
| | Tube diameter, $d_t$, [mm] | 31, 41, 61 |
| | Number of face mesh per pellet [#] | 3120 |
| Cylinders | Pellet size [mm] | $d_p/h_p$: 10, $d_{pv}$: 11.45 |
| | Tube diameter, $d_t$, [mm] | 22.9, 35.5, 45.8 |
| | Number of face mesh per pellet [#] | 4400 |
| Raschig rings | Pellet size [mm] | $d_{po}/d_{pi}/h_p$: 10/6/10, $d_{pv}$: 9.87 |
| | Tube diameter, $d_t$, [mm] | 30.6, 40.5, 60.2 |
| | Number of face mesh per pellet [#] | 8008 |
| Surface friction coefficient (dynamic) for pellets/tube wall | | 0.1/0.6 |
| Surface bounciness (COR*) for pellets/tube wall | | 0.9/0.6 |
| Gravity acceleration [m $s^{-2}$] | | 9.81 |
| Integration time step bounds [s] | | [0.0025–0.025] |

* COR: Coefficient of Restitution.

### 2.2. Fully resolved CFD simulations

CAD models of the packing structures are generated by importing the RBD-generated topology into ANSYS Workbench 18.2. To avoid generating highly skewed cells in the contact regions, we shrink the pellets by 0.5% around their respective centres of mass, resulting in very small interstices at the contact points. An advanced meshing approach is implemented based on a combination of patch-independent and patch-conforming meshing methods to generate a high quality inflationary mesh topology in the dense packing structures. This is conducted by an ad-hoc Python script in ANSYS Workbench 18.2, which creates very fine meshes at the contact regions (with the size of $d_p/200$) growing into coarser tetrahedral grids in the bulk of voids and particles (with the size of $d_p/18.2$) through a graded meshing scheme. The generated mesh is then further modified with six prismatic layers with an initial height of $2.5 \times 10^{-6}$ m and a growth factor of 1.2 of thickness per layer along the surface normal direction, resulting in $y^+ \approx 1$ according to the Enhanced Wall Treatment (EWT) method. Further details about the meshing procedure along with the mesh refinement study have been elaborated and investigated in our previous studies, i.e. Moghaddam et al. (2019, 2020). Fig. 3 illustrates typical results of the graded volume mesh generated in packing of rings with $N_{pv}$ = 3.1.

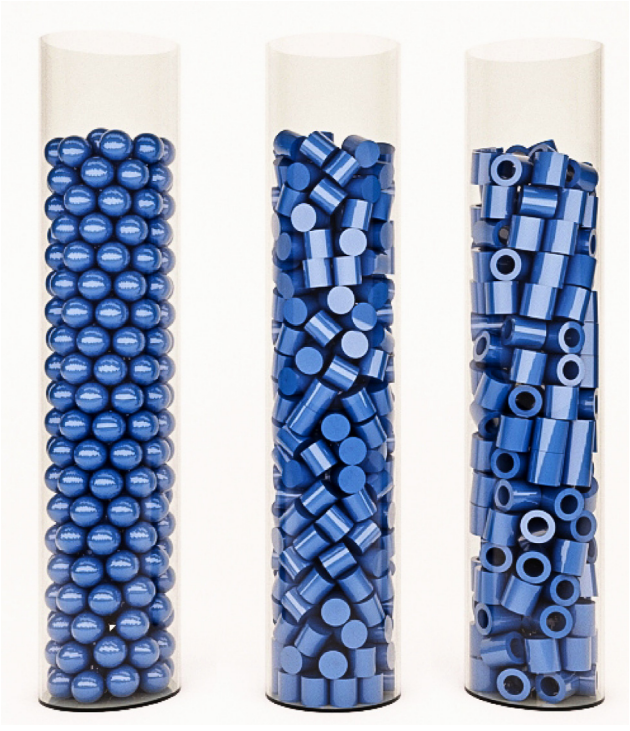

**Fig. 2.** Computer–generated structures using RBD algorithm for spheres, cylinders and Raschig rings with N = 4.1, 4.58 and 4.05, respectively.

3D Discrete-pellet CFD simulations of flow and heat transfer for a wall-heated fixed bed reactor problem are performed for packing models described in Table 1 for the laminar, transitional and turbulent flow regimes, using the finite volume code ANSYS Fluent 18.2. Air as the standard fluid at total pressure of 1.01325 bar and a temperature of 298 K, which gives the physical properties of $\rho$ = 1.22 5 kg/$m^3$, $c_p$ = 1006.43 J/kg.K, $k_f$ = 0.0242 W/m.K, $\mu = 1.7894 \times 10^{-5}$ Pa.s (yielding a molecular Prandtl number of 0.74) is introduced to the bottom of the computational domain at uniform axial velocity and temperature to provide a constant basis for further comparisons and analysis. At the flow entry, a velocity-inlet boundary condition is considered with axial velocity giving $Re_p$ (based on the volume-equivalent particle diameter) ranging from 5 to 3000. Furthermore, the initial inlet turbulence intensity is calculated based on the formula $I = 0.1Re^{-1/8}$. The thermal boundary condition at the tube wall is considered as constant temperature ($T_w$ = 700 K for $Re_p \leq 200$ and $T_w$ = 1500 K for $Re_p \geq 400$). The thermal conductivity of the pellets is set as 1.01, 16.27 and 40 W/m.K, corresponding to glass, steel and alumina catalyst material, respectively. A schematic drawing of the CFD model and boundary condition is given in Fig. 3. For discrete-pellet CFD simulations, the three-dimensional compressible Navier-Stokes and energy equations together with conjugate heat transfer model to account for the interphase heat transfer rate for the laminar flow regime ($Re_p \leq 100$) are solved. For the fully-turbulent flow regime, i.e. for $Re_p \geq 600$, the realizable k-ε model combined with the Enhanced-Wall-Treatment is applied, which basically is a verified Reynolds-averaged Navier–Stokes (RANS) model for simulating velocity and temperature fields with strong streamline curvature (see e.g. Guo et al., 2019; Moghaddam et al., 2019). The rate models are then solved using the pressure-based segregated solver in ANSYS Fluent 18.2, with the SIMPLE (Semi-Implicit Method for Pressure Linked Equations) algorithm for pressure–velocity coupling and the PRESTO! (PREssure STaggering Option) interpolation scheme to estimate cell-face pressure, along with a second-order upwind interpolation method to interpolate the field variables. The CFD runs are initially set under isothermal conditions with only momentum and turbulence activated. Having obtained a converged velocity field, the heat transfer simulations are run by setting the thermal boundary conditions and the temperature-dependent properties of the flowing medium.

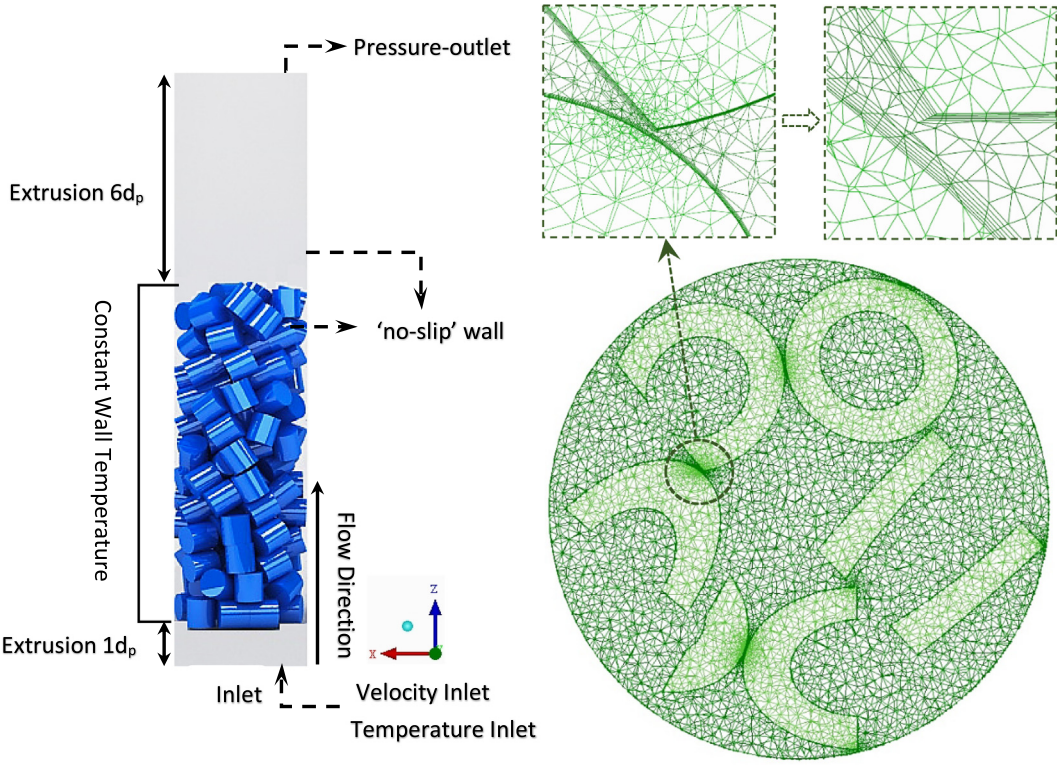


**Fig. 3.** Left: schematic drawing of the CFD flow model along with boundary conditions used for 3D discrete-pellet CFD simulations represented by a tube packed with equilateral cylinders with N = 4.58. Right: typical results of graded volume mesh topology (at height z = $5d_p$) in a packing of rings with $N_{pv}$ = 3.1.

## 3. 2D Pseudo-homogenous heat transfer model

Conceptually, when using 2D pseudo-homogenous heat transfer models, we translate the transport processes taking place in a 3D two-phase gas–solid system into a 2D scale represented by a quasi-homogenous medium. This requires "effective" parameters that reflect the underlying transport mechanisms occurring in fluid and pellet phases. In fact, the model describes the overall heat transfer resistance by an effective radial thermal conductivity, $k_{er}$, lumping together all heat transfer mechanisms in the radial direction, and an apparent wall heat transfer coefficient, $h_w$, which is postulated to account for the temperature jump near the wall region. These parameters are obtained by resorting to the inverse problem, using the pseudo-homogeneous heat transfer model to predict the observed (and suitably averaged) temperature field data.

Here, the 2D-ADPF heat transfer model, Eq. (1), is considered as the fitting model. The objective of this analysis is to compute the effective radial thermal conductivity, $k_{er}$, and apparent wall heat transfer coefficient, $h_w$, for an entire fixed bed of a certain length, using a multivariable optimization routine such that the best fit between the 2D-ADPF heat transfer model results and CFD results of heat transfer is achieved. The 2D-ADPF heat transfer model is presented in the following dimensionless form:

$$\frac{\partial\theta}{\partial\zeta}=\frac{1}{Pe_{er}}\left(\frac{2}{N}\right)\left(\frac{\partial^2\theta}{\partial\omega^2}+\frac{1}{\omega}\frac{\partial\theta}{\partial\omega}\right)+\frac{1}{Pe_{ea}}\left(\frac{2}{N}\right)\left(\frac{\partial^2\theta}{\partial\zeta^2}\right) \tag{1}$$

with the following boundary conditions:

$$for\ \zeta=0:\ \theta=1 \tag{2}$$

$$for\ \omega=0:\ \frac{\partial\theta}{\partial\omega}=0 \tag{3}$$

$$for\ \omega=1:\ \frac{\partial\theta}{\partial\omega}+Bi\theta=\begin{cases}Bi\ (\zeta>0)\\ 0\ (\zeta<0)\end{cases} \tag{4}$$

where $\zeta = z/R_t$ is the dimensionless axial position and $\omega = r/R_t$ the dimensionless radial position, non-dimensionalized by the tube radius $R_t$, and $\theta = (T_w - T)/(T_w - T_0)$ is the dimensionless temperature, non-dimensionalized by the difference between wall and inlet gas temperatures $T_w$ and $T_0$. The radial and axial heat dispersion is characterized by the effective radial and axial Peclet numbers $Pe_{er} = Gc_pd_{pv}/k_{er}$ and $Pe_{ea} = Gc_pd_{pv}/k_{ea}$, with G the mass flux. The wall-to-bed heat transfer is characterized by the Biot number $Bi = h_wR_t/k_{er}$. The 2D-ADPF heat transfer model has an analytical solution in terms of an infinite series of Bessel functions, which can be obtained using the Fourier method (Gunn and Khalid, 1975; Wakao et al., 1979):

$$\frac{T_w-T(\zeta,\omega)}{T_w-T_0}=\theta(\zeta,\omega)=2\sum_{i=1}^{\infty}\frac{J_0(\lambda_i\omega)\exp(-\lambda_i^2\gamma)}{\lambda_i\left[1+(\lambda_i/Bi)^2\right]J_1(\lambda_i)} \tag{5}$$

where

$$\gamma=\frac{4\zeta\frac{1}{Pe_{er}}\frac{1}{N}}{1+\sqrt{1+16\lambda_i^2\frac{1}{Pe_{er}}\frac{1}{Pe_{ea}}\frac{1}{N}}} \tag{6}$$

and the eigenvalues $\lambda_i$ are the roots of the characteristic equation:

$$\lambda_iJ_1(\lambda_i)-BiJ_0(\lambda_i)=0 \tag{7}$$

To examine if the procedures proposed by Dixon (2012, 1985) and the Borkink and Westerterp research group, i.e. Borkink (1994) and Borkink and Westerterp (1992), are able to resolve the problem of length-dependency, the inlet gas temperature that is needed to make a dimensionless temperature profile is computed based on two methods: (i) the mass weighted-average

(mixing-cup) temperature at the bed inlet, which is calculated by Eq. (8), and (ii) the azimuthally-averaged radial temperature profile at the bed inlet, i.e. $T_0(\omega)$.

$$\bar{T}_0 = \frac{\int T\rho|\boldsymbol{v}.d\boldsymbol{A}|}{\int \rho|\boldsymbol{v}.d\boldsymbol{A}|} = \frac{\sum_{i=1}^{n} T_i\rho_i|\boldsymbol{v}_i.d\boldsymbol{A}_i|}{\sum_{i=1}^{n} \rho_i|\boldsymbol{v}_i.d\boldsymbol{A}_i|} \tag{8}$$

The observed data to be employed in our multi-variable parameter estimation problem includes the azimuthally-averaged temperature profile obtained from CFD simulations of heat transfer for all case studies (see Table 1) for which the heat transfer simulations are performed for inlet flow conditions corresponding to $Re_p$ = 5, 10, 50, 100, 200, 400, 600, 800, 1000, 2000, 3000, further repeated for three different pellet materials. This allows access to an extensive data pool of temperature fields in packing structures of spheres, cylinders and Raschig rings with different tube-to-pellet ratios $N$, and for a wide range of particle Reynolds numbers, $5 \leq Re_p \leq 3000$. Furthermore, to investigate the influence of bed length on $k_{er}$ and $h_w$, azimuthally-averaged temperature data at different bed cross sections z = $1d_p$, $3d_p$, $5d_p$, $7dv$, $9d_p$, $10d_p$ to $11d_p$ (representing the end of the packing section) and $+2d_p$ behind the packing section are utilized to solve the parameter estimation problem. Fig. 4 illustrates the different bed cross sections and shows schematically the procedure to obtain an azimuthally averaged temperature profile. For each cross section, a number of circles of different radii, with an increment of size $d_p/10$, cutting through both fluid and solid cells, is drawn. Then a line-averaged temperature for each circle is measured, averaging over both fluid and solid phases, thereby computing the radial temperature profile at a typical cross section. This way the temperature field data at different cross sections can be translated into 2D radial temperature profiles, which can be compared with the pattern predicted by Eqs. (5)–(7). It is worth noting that in our optimization procedure we do not aim to determine *local* effective parameters. Rather, for each specific cross-section we aim to determine the set of *global* (volume-averaged) effective parameters which, when applied to the entire volume from the entrance of the fixed bed to that specific cross section, yields the same azimuthally-averaged (radial) temperature profile as in the azimuthally-averaged of 3D temperature fields extracted from CFD results.

Before proceeding to the solution, it is essential to discuss the role of the axial Peclet number, $Pe_{ea}$. Wakao et al. (1978) demonstrated that the influence of $Pe_{ea}$ on the minimum error obtained

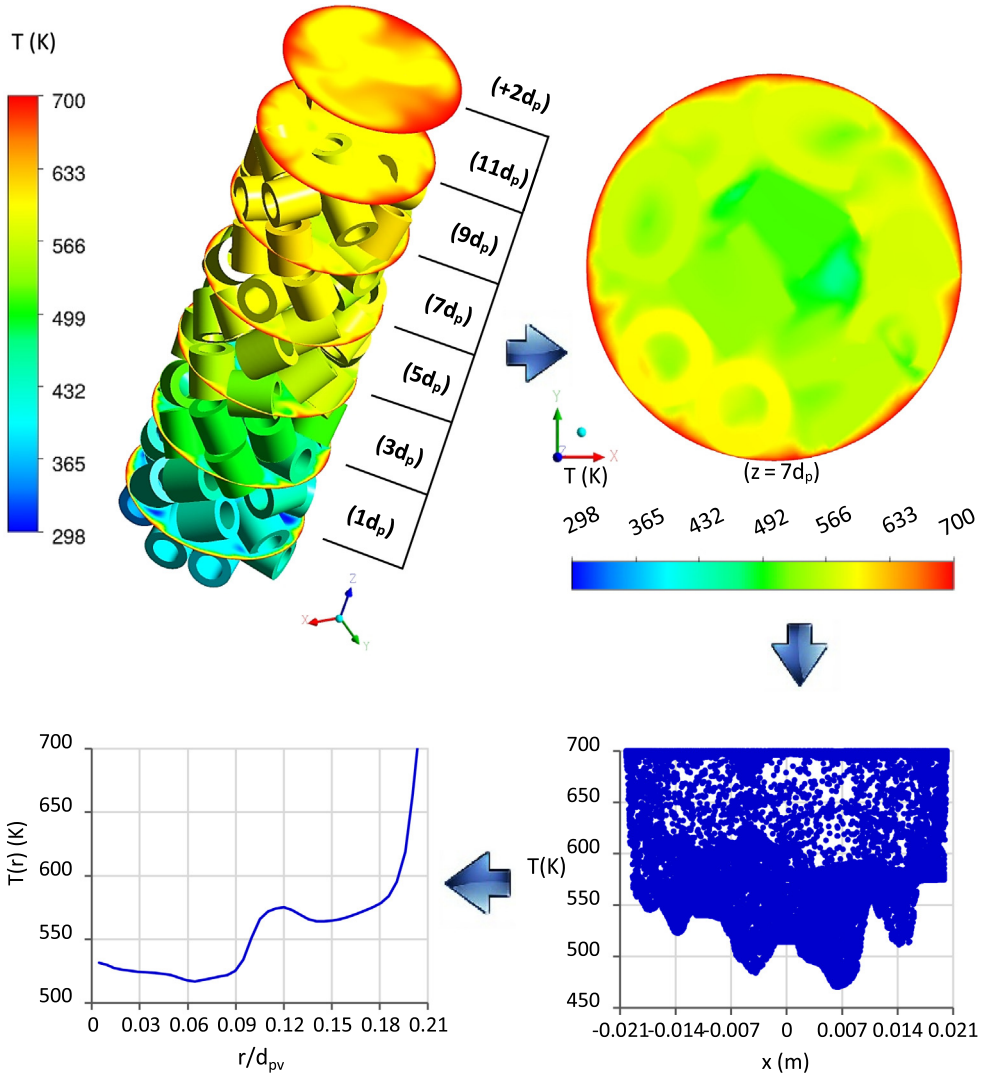


**Fig. 4.** General sequence to obtain the azimuthally-averaged temperature distribution at different cross sections for random packings of alumina Raschig rings with N = 4.05 at $Re_p$ = 100. In this example, we focus on the cross section at axial position z = $7d_p$, shown top right. Bottom right: individual temperature measurements (here local data is shown as a function of x-coordinate, but note that in the actual procedure all local data at the same radial position r is used). Bottom left: azimuthally averaged radial temperature profile.

from their model optimization is negligible. This explains why it is possible that some literature values for $k_{ea}$ are larger than any realistic value by an order of magnitude, see e.g. Li and Finlyson (1976) and Paterson and Carberry (1983). Overall, there are no severe comments found in the literature that address any shortcomings or discrepancies on the published correlations for the axial heat transfer Peclet number. Therefore, in this work, $Pe_{ea}$ is kept constant and computed from the empirical correlation proposed by Dixon and Cresswell (1979), assuming $Pe_{af(\infty)} = 2$, and using the correlation presented by Zehner and Schlünder (1973) for the effective solid conductivity.

$$\frac{1}{Pe_{ea}} = \frac{1}{Pe_{af(\infty)}} + \frac{k_{as}}{k_f}\frac{1}{Re_p \mathrm{Pr}} \tag{9}$$

where

$$\frac{k_{as}}{k_f} = 1 - \sqrt{1-\varepsilon} + \frac{2\sqrt{1-\varepsilon}}{(1-\frac{k_f B}{k_p})}\left[\frac{(1-\frac{k_f}{k_p})B}{(1-\frac{k_f B}{k_p})^2}\ln(\frac{k_p}{k_f B}) - \frac{B+1}{2} - \frac{B-1}{(1-\frac{k_f B}{k_p})}\right] \tag{10}$$

$$with\ B = C(\tfrac{1-\varepsilon}{\varepsilon})^{10/9}$$

and C is 1.25, 2.5, $2.5(1+(d_i/d_o)^2)$ and 1.4 for spheres, solid cylinders, and hollow cylinders, respectively. In Eq. (9), *Pr* is the Prandtl number defined as $\mu c_p/k_f$.

To compute $Pe_{er}$ and *Bi*, we applied a nonlinear least squares (NLLS) method, which uses an initial guess for the effective parameters, whereby the radial temperature profile is predicted using Eqs. (1)–(10) at locations corresponding to the measurements, i.e. at a specific cross section where the azimuthally-averaged temperature data is obtained. The parameters are then altered using a multi-variable optimization approach to minimize the sum of squares of the differences, giving the best-fit parameter estimates. The objective function in this optimization problem is therefore an error function, which is the root of the mean square error between the predictions and measurements.

$$Error = \left[\frac{1}{n}\sum (T_{Pre} - T_{CFD})^2\right]^{1/2} \tag{11}$$

where $T_{Pre}$ and $T_{CFD}$ are the predicted and measured temperatures, respectively, and n is the total number of points of comparison at the specified cross section. The effective parameters corresponding to the minimum error represent the best that can predict the measured temperatures, i.e. azimuthally-averaged temperature profile obtained from the CFD results. To obtain the global minimum, a robust optimization function, FMINCON, available in Matlab is used, which enables us to compute a constrained minimum of a scalar function of several variables starting at an initial guess. A detailed description as well as the background of this nonlinear optimization function can be found in standard references (Byrd et al., 2000; Coleman and Li, 1996; Waltz et al., 2006). It is worth mentioning that a robust optimization routine must be adopted because, first, our problem includes functions with strong nonlinear dependencies on the variables, and secondly, both $Pe_{er}$ and *Bi* have a limited range of values, enabling the optimization solver to narrow down the search regions, and accordingly reduce computational expenses.

To make a reasonable initial guess for $Pe_{er}$ and *Bi*, the empirical correlations proposed by Melanson and Dixon (1985) and Dixon et al. (1978) are used. Despite the observed scattering of the predicted values of $Pe_{er}$ and $Nu_w$ versus $Re_p$ based on different literature correlations, these parameters appear to vary within certain range. To this end, we assume the values of $Pe_{er}$ and $Bi(d_p/R_t)$ should be within the range of [0.1–15] and [1–10], respectively. Furthermore, the physical properties of air are calculated at the average temperature at a specific cross section. To ensure that the computed values by the FMINCON function addresses the global minimum of our objective function, we also examined another nonlinear least-squares solver programmed in Matlab, LSQNONLIN, which solves nonlinear least-squares curve fitting problems. The background of this algorithm is elaborated in Coleman and Li (1996).

## 4. Results and discussion

Effective parameter optimization has been conducted for 168 case studies, including the packing structures of spheres, cylinders and Raschig rings with different *N* for the full range of $Re_P$ and different pellet materials to investigate the effect of bed length on the effective heat transfer model parameters, i.e. $k_{er}$ and $h_w$.

### 4.1. Verification study

To assure that the FMINCON optimization results reflect the global minimum of the objective function, we first compared its predictions with LSQNONLIN. The computed values of $Pe_{er}$ and *Bi* based on both solvers are very comparable: the difference is in the third decimal digit.

To measure the accuracy of the optimization results, the observed temperature data, i.e. azimuthally-averaged temperature profiles obtained from the RBD-CFD heat transfer results, are compared with the radial temperature profiles predicted by the 2D-ADPF heat transfer model, based on the optimum values of $Pe_{er}$ and *Bi* in Fig. 5. The figure exhibits a comparison at different bed cross sections in random packings of alumina Raschig rings with N = 4.05 and 6.02 at $Re_p = 100$. Clearly, the radial temperature profile predicted by the 2D-ADPF heat transfer model does not show the hump shape observed in the azimuthally-averaged temperature profile. This is caused by the fact that, in addition to the plug flow idealization, the model basically presumes no thermal resistance between fluid and pellet phases (implying neglect of granularity on the pellet scale). The 2D-ADPF heat transfer model is basically unable to reflect the role of thermal disequilibrium between individual phases along both the tube radius and reactor depth. A better fit can be foreseen at higher bed cross sections where thermal equilibrium has (almost) been reached between both phases, and thus the assumption of no thermal resistance between the two phases is legitimate. Indeed, the results demonstrate that when the two phases approach thermal equilibrium, as can be realized at $z = 9d_p$, a better prediction of the radial temperature profile is possible by the 2D-ADPF model. Nevertheless, as shown in Fig. 6, azimuthal averaging of 3D temperature field to generate 2D radial temperature profile leads to a large deviation from local data. The maximum deviations of the local temperature data from $T(r,z = 4.5d_p)$ are 103 K and 187 K observed at $(R_t-r)/d_{pv}$ = 0.43 and 1 for packings of rings with *N* = 3.1 and 6.1, respectively.

### 4.2. Influence of the inlet temperature profile

Here, we explore whether the suggestion by Dixon (2012, 1985) and Borkink and Westerterp (1994, 1992), i.e. to use a radially dependent inlet temperature profile $T_0(\omega)$ in Eqs. (1)–(7) instead of a constant inlet temperature profile, can explain the reactor length effect. To this end, we performed several optimization runs using both a mass-weighted average (flat profile) inlet temperature and radially dependent inlet temperature $T_0(r)$ for a case study including random packing of alumina spheres with N = 3.1 at $Re_p$ = 10, 100 and 1000. Here, for sake of brevity, only the results at $Re_p = 100$ are presented in Fig. 7, where the computed values of $Pe_{er}$ are compared and benchmarked against the predictive correlation of Melanson and Dixon (1985).

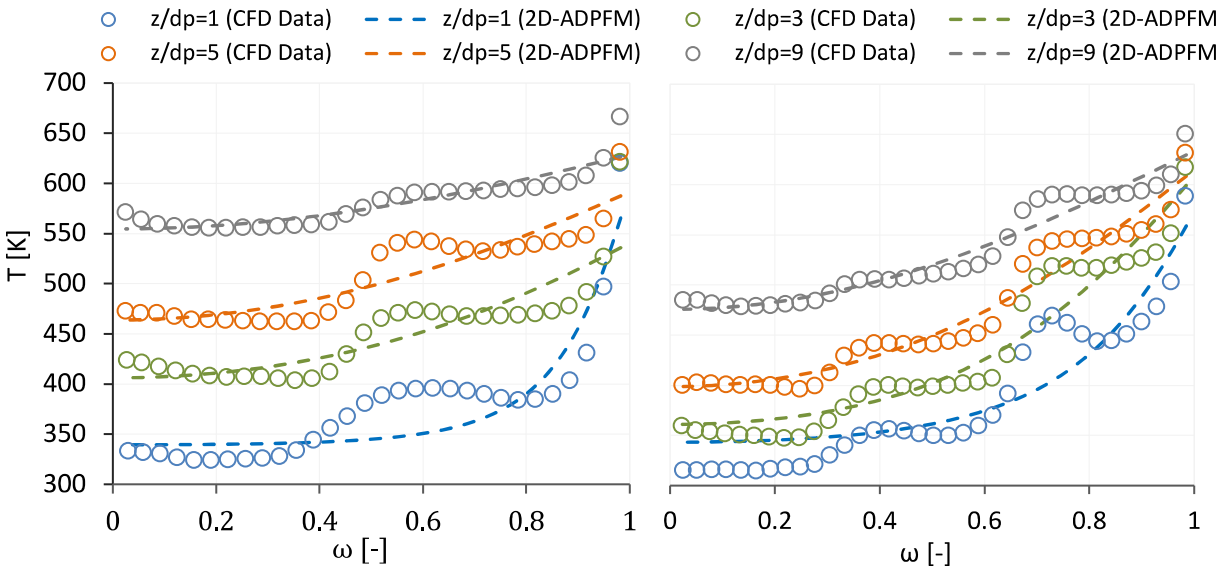


**Fig. 5.** Comparison between the azimuthally-averaged temperature profiles obtained from RBD-CFD results and the radial temperature profile predicted by the 2D-ADPF heat transfer model at cross sections z = $1d_p$, $3d_p$, $5d_p$ and $9d_p$ in random packings of alumina Raschig rings with: (a) $N$ = 4.05 and (b) 6.02, at $Re_p$ = 100.

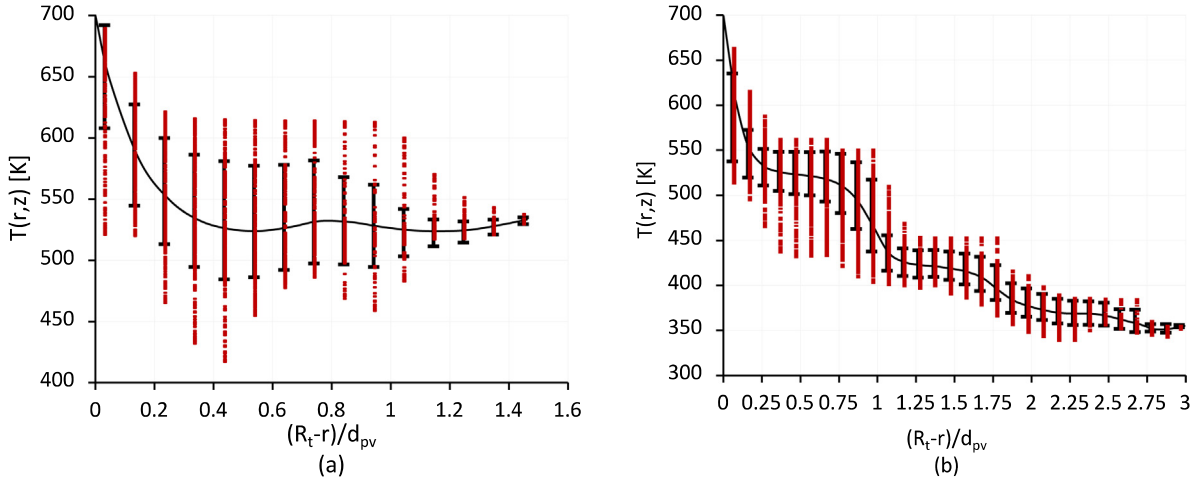


**Fig. 6.** Comparison between the azimuthally-averaged temperature (lines) and local temperature data sampled from different azimuthal positions (red dots, standard deviations quantified by black bars) at cross section z = $4.5d_p$ in alumina Raschig rings packings: (a) with $N$ = 3.1 and (b) with $N$ = 6.1 at $Re_p$ = 100. (For interpretation of the references to color in this figure legend, the reader is referred to the web version of this article.)

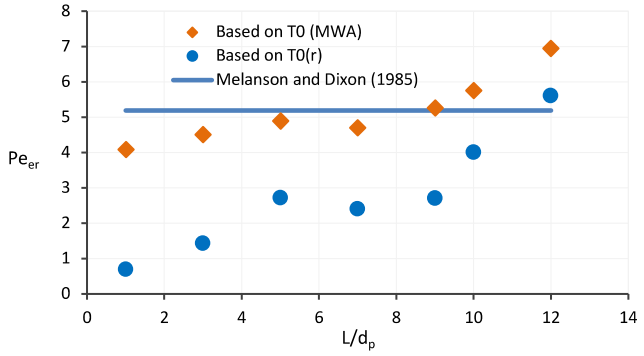


**Fig. 7.** Comparison between computed effective radial Peclet number $Pe_{er}$ based on different inlet temperature profiles for random packing of alumina sphere with $N$ = 3.1 at $Re_p$ = 100.

As shown in Fig. 7, no matter by which method the inlet temperature in the 2D-ADPF model is introduced, the results still show the length dependency of $Pe_{er}$. Furthermore, applying $T_0(r)$ leads to an underestimation of $Pe_{er}$ by around 200% compared to the predicted values by the Melanson-Dixon correlation. Similar results have been found for $Bi$ and both $Pe_{er}$ and $Bi$ at $Re_p$ = 1000. This means that the length-dependency of the effective heat transfer parameters cannot be explained or circumvented by using $T_0(r)$ instead of a flat temperature profile, and conceptually does not stem from experimental errors per se. It is worth remarking that the predicted values of $Pe_{er}$ and $Bi$ at $Re_p$ = 10 are the same between the two approaches, which is explained by the fact that the radially dependent temperature profile approaches a flat profile as $Re_p \rightarrow 0$.

### 4.3. Influence of pellet shape and tube-to-pellet size ratio

The behavior of the volume-averaged $k_{er}$ and $h_w$ as a function of bed length is shown in Figs. 8 and 9, respectively, for all packing structures at three values of $Re_p$, representative for laminar, transient and turbulent flow regimes. Overall, the displayed graphs demonstrate that the computed values of $k_{er}$ and $h_w$ vary with

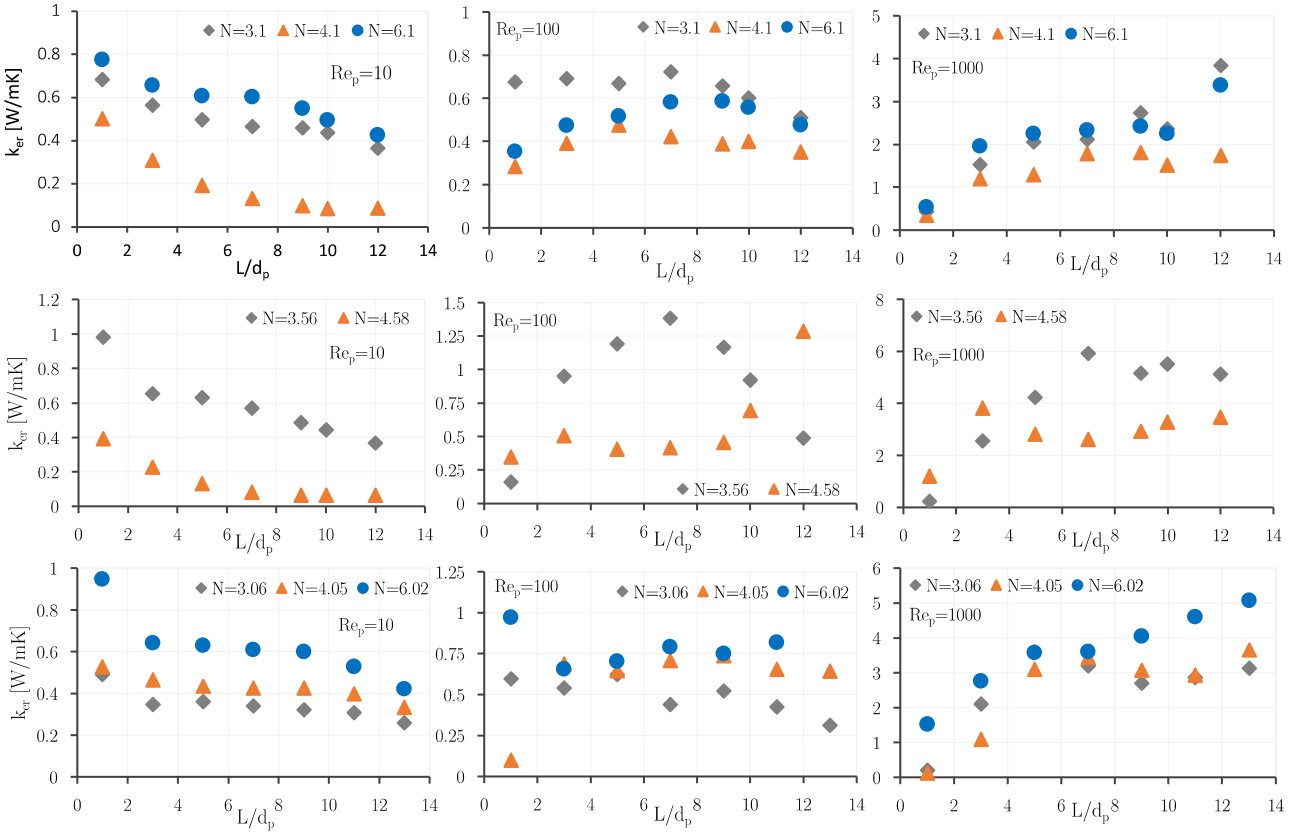


**Fig. 8.** Influence of bed height and $N$ on $k_{er}$ in random packings of spheres (first row), cylinders (second row) and Raschig rings (third row).

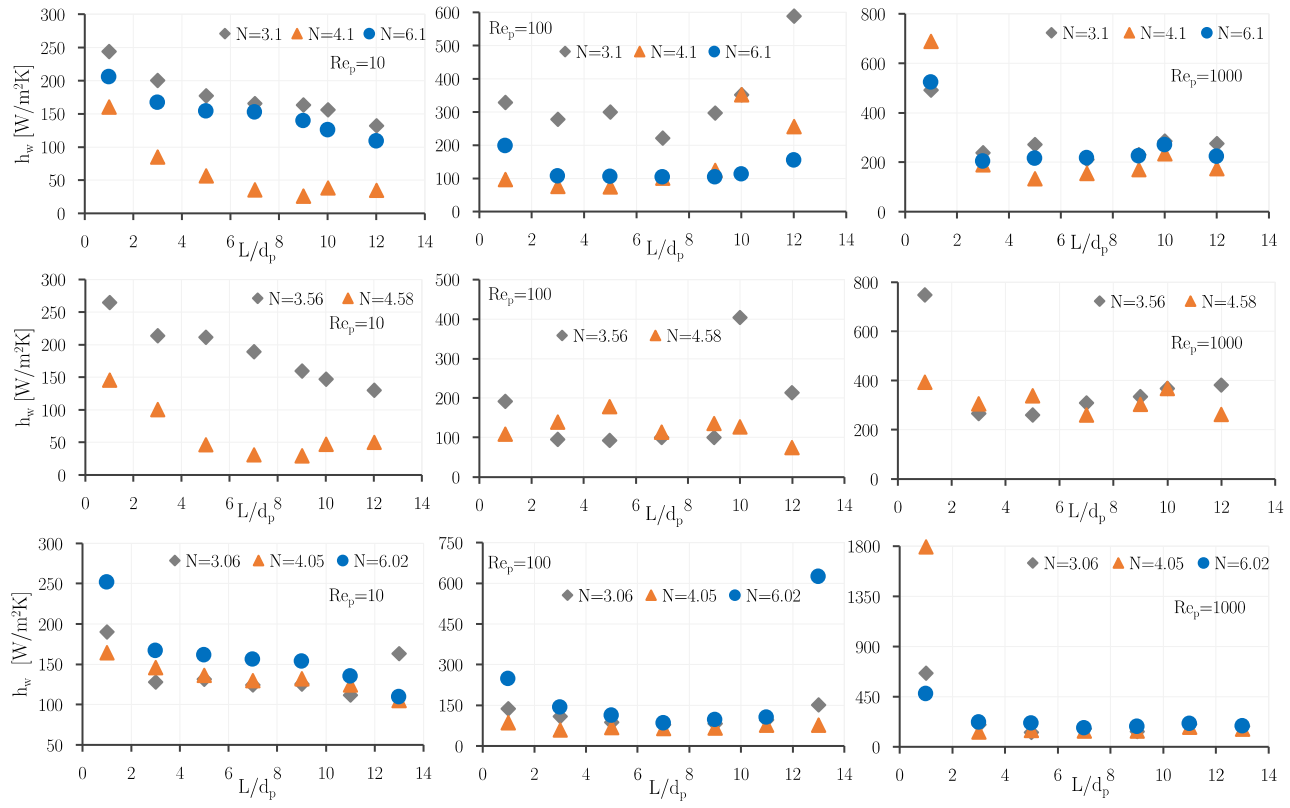


**Fig. 9.** Influence of bed height and $N$ on $h_w$ in random packings of spheres (first row), cylinders (second row) and Raschig rings (third row). This increasing trend can be explained by the increasing role of eddy transport along the bed, which can be represented by the change of turbulent intensity and/or turbulent kinetic energy along the bed (see Fig. 10).

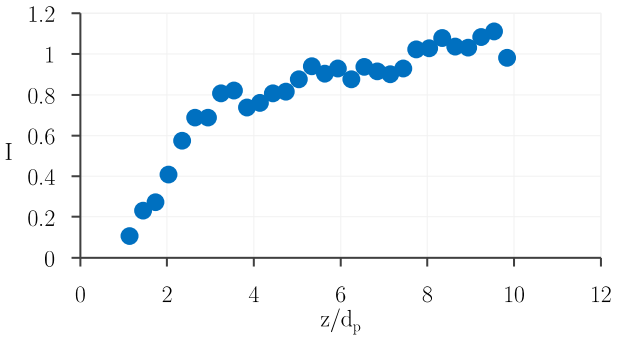


**Fig. 10.** Averaged axial turbulent intensity profile as a function of axial position in a random packing of alumina Raschig rings with N = 4.05 at $Re_p$ = 1000.

bed length, and this length-dependent behavior does not pertain to pellet shape, thermal conductivity or tube-to-pellet diameter ratio. The length-dependency is observed, despite the fact that the observed data has been obtained from our RBD-CFD simulations, thereby completely avoiding the prevailing shortcomings connected to conventional experimental analysis, i.e. heat leaks into calming sections as well as heat losses from thermometers, as presumed by Dixon (1985). This result, again, demonstrates that procedures suggested by Dixon (2012, 1985) and Borkink and Westerterp (1994, 1992) cannot unravel and solve the problem of the bed length-effect (see Fig. 10).

As shown in Fig. 8, the graphs exhibit different patterns concerning the behavior of $k_{er}$ versus the length of packing section. In the laminar flow regime, $k_{er}$ shows a decreasing trend as a function of bed length progression, and eventually approaches an asymptotic value (see Fig. 8 for plots at $Re_p$ = 10 as a representative of laminar flow regime). Similar trends have been found for all cases at $Re_p$ < 100. This result is in agreement with the observations by de Wasch and Froment (1972), Gunn and Khalid (1975) and Dixon (1985). In the transient flow regime, which is expected to occur at $Re_p$ in the range of 100 or 200–600 (although it seemingly depends on $N$), the behavior of $k_{er}$ as a function of bed length does not reach a discernable trend (see Fig. 8 for plots at $Re_p$ = 100 as a representative of the transient regime). This behavior can be attributed to the formation of local vortices, which partially emerge along the packing section, resulting in scattering of the $k_{er}$ data with an intractable trend. For $Re_p$ higher than 600, i.e. in the fully turbulent regime, $k_{er}$ is shown to increase to an asymptotic value as the bed length increases (see Fig. 8 for plots at $Re_p$ = 1000 as a representative of the turbulent regime).

Nonetheless, a reliable interpretation regarding the trend of $k_{er}$ for the turbulent flow regime requires much longer beds, so that the residence time of the flowing fluid is high enough to allow both phases to reach thermal equilibrium.

The results depicted in Fig. 8 demonstrate a very poor radial heat transfer in the packing structures that include an axial hole, e.g. packing of spheres, cylinders and Raschig rings with $N$ = 4.1, 4.58 and 4.05, respectively, where the computed values of $k_{er}$ are clearly lower than for other cases. Neglecting such structures from our window of analysis, the results generally show that $k_{er}$ increases as $N$ increases in the laminar flow regime (see Fig. 8 for $Re_p$ = 10 as a representative), whilst in the transient and turbulent regimes the computed values for $k_{er}$ are comparable, making it difficult to find a correlation between $k_{er}$ and $N$. Nonetheless, there is a very limited number of published correlations that account for the influence of $N$ on $k_{er}$ at low $Re_p$.

The results highlighted in Fig. 8 also confirm the advantage of shaped pellets for improving the wall-to-bed heat transfer rate, as the computed values of $k_{er}$ are higher for packings of cylinders and Raschig rings than for packings of spheres.

Fig. 9 shows that, in general, the apparent wall heat transfer coefficient $h_w$ decreases as a function of bed length, apparently approaching an asymptotic value, with much smoother trends compared to $k_{er}$. Several other researchers have reported similar patterns for $h_w$ based on their experimental and theoretical analyses (de Wasch and Froment, 1972; Dixon et al., 1978; Dixon, 1985; Gunn and Khalid, 1975). To explain the length-dependent behavior of the apparent wall heat transfer coefficient, we look into the trend of wall heat flux along the bed depth. Results of azimuthally-averaged wall heat flux are depicted as a function of axial position in Fig. 11 for a random packing of alumina Raschig rings with $N$ = 4.05 at $Re_p$ = 10, 100 and 1000.

The apparent wall heat transfer coefficient as a function of bed length is correlated with the axial trend of the wall heat flux in conjunction with the trend of radial heat dispersion along the bed. This can be expressed through the boundary condition of heat transfer at the tube wall, i.e. Eq. (4), wherein the apparent wall heat transfer coefficient plays the role of a thermal resistance to account for the so-called temperature jump. This equation can be rewritten in dimensional form as:

$$q_w = h_w(T_w - T) = k_{er}\frac{\partial T}{\partial r} \tag{12}$$

Fundamentally, the fluid and catalyst solid phases approach thermal equilibrium for sufficiently long beds, i.e. $T_f \rightarrow T_s \rightarrow T_w$ as $z \rightarrow \infty$, thereby reducing the wall heat flux to the bed, as shown in Fig. 11. This explains why, for example, in the laminar flow regime both $h_w$ and $k_{er}$ decrease along the bed depth. In this case, the reduction of $k_{er}$ as a function of bed length implies that the decreasing rate in the wall heat flux would have been higher than the decreasing rate of the radial temperature gradient, and accordingly ($T_w$ -T) along the bed, thereby causing a decreasing trend for $h_w$ along the packing length. It is consequently evident that in turbulent and transient flow regimes, the behavior of $h_w$ as a function of bed length would also be governed by the simultaneous behavior of the effective radial thermal conductivity and wall heat flux. Since there is a strong connection between the wall heat flux and the thermal equilibrium condition at a specific axial position in the bed, it can be deduced that the length-effect phenomenon stems from the trend of temperature non-equilibrium along the bed length. Reiterating that 2D pseudo-homogenous models are based on the thermal equilibrium assumption between fluid and catalyst phases, the effective thermal parameters thus need to capture effectively how far the two phases are from local thermal equilibrium, as well as the radial heterogeneity in the bed structure and local flow mal-distribution.

Note that, as in the case of $k_{er}$, the presence of a channel near the center of the some of the packing structures leads to a poor heat transfer rate in the wall region. This is reflected in Fig. 9 by the lower values of the apparent wall heat transfer coefficient for random packings of spheres, cylinders and Rachig rings with N = 4.1, 4.58 and 3.06, respectively, in all flow regimes. In fact, the presence of a flow channel reduces the radial dispersion in a packed column, thereby reducing the radial heat transfer rate, which is quantitatively evidenced here by the lower values of $k_{er}$ and $h_w$. Based on these results, we cannot find a correlation between $h_w$ and $N$ which is in conformity with the published correlations, because none of the known correlations account for the role of $N$.

It is remarkable to find that results depicted in Fig. 9 do not show a major influence of the pellet shape on $h_w$ (contrary to the results found for $k_{er}$), which means that the rate of heat transfer at the wall region cannot be improved by the use of non-spherical pellets. This observation can be explained by the high local porosity (for any pellet shape) at the wall region, which implies a dominance of convection mechanisms in this region.

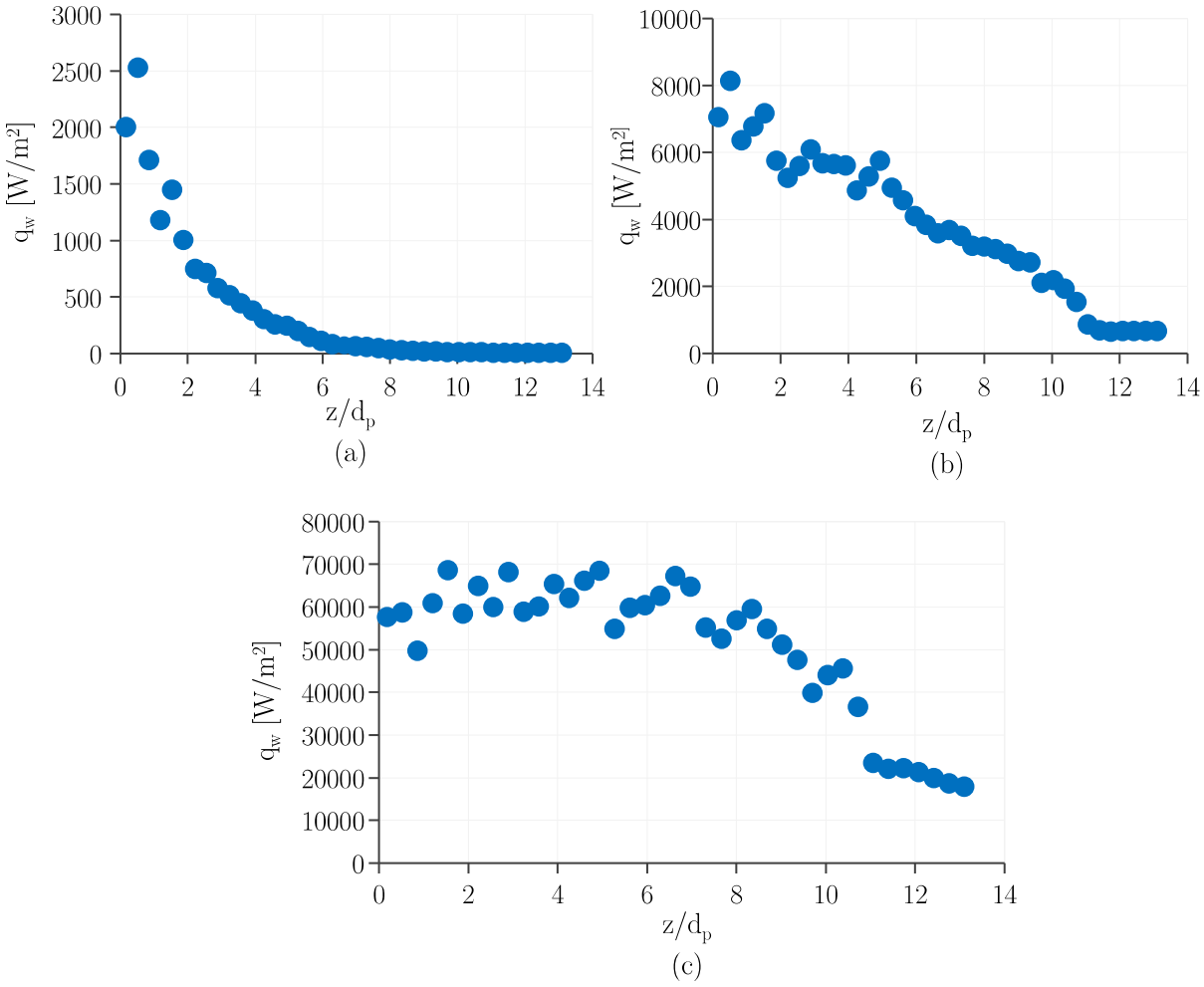


**Fig. 11.** Azimuthally-averaged axial profile of wall heat flux in a random packing of alumina Raschig rings with $N$ = 4.05; (a) $Re_p$ = 10, (b) $Re_p$ = 100 and (c) $Re_p$ = 1,000.

### 4.4. Influence of pellet thermal conductivity

To investigate the role of pellet thermal conductivity on the effective heat transfer parameters, we now turn to fixed beds with pellets of different thermal conductivities, namely of alumina and glass. We investigate different shapes with $N$ = 3.1 at $Re_p$ = 10, 100 and 1000. The results for $k_{er}$ and $h_w$ are depicted as a function of bed length in Figs. 12 and 13, respectively.

Generally, the results show a large influence of the pellet's thermal conductivity on the effective radial thermal conductivity in all flow regimes (see Fig. 12), while the influence on the apparent wall heat transfer coefficient can only be recognized at low $Re_p$ (see Fig. 13). The first observation highlights how remarkably important is the role of stagnant contributions to $k_{er}$, even for transient and turbulent regimes. This reflects the sizeable contribution of radial conduction within the catalyst phase to the radial heat dispersion. The second observation is in agreement with the presence of a high local porosity in the wall region, which suggests dominance of convective mechanisms. This justifies our observation that $h_w$ does not depend on the pellet's thermal conductivity at high $Re_p$, say $Re_p$ > 100. Nonetheless, it seems that at low $Re_p$ the role of conductive transport at the wall region becomes important (see Fig. 13 for $Re_p$ = 10).

### 4.5. Reliability and accuracy of literature correlations

Finally, we inspect the reliability and accuracy of classical $k_{er}$ - $h_w$ heat transfer models in predicting the wall-to bed heat transfer rate. To this end, the radial temperature profiles predicted by the 2D-ADPF heat transfer model based on different sets of literature correlations are compared to the azimuthally-averaged temperature data from the RBD-CFD simulation results. In spite of a multiplicity of choices with evidently conflicting results, we have employed the often-cited correlations used in design computations, embracing those proposed by the "schools" of Yagi/Kunii/Wakao (Yagi and Kund, 1964; Yagi and Kunii, 1957; Yagi and Wakao, 1959), Zehner/Bauer/Hennecke/Schlünder (Bauer and Schlunder, 1978; Hennecke and Schlünder, 1973; Zehner and Schlünder, 1973, 1970), Specchia/Baldi/Gianetto/Sicardi (Specchia et al., 1980, 1978), Cresswell/Dixon/Paterson (Dixon and Cresswell, 1986, 1979; Dixon et al., 1978; Dixon, 1988; Melanson and Dixon, 1985) and Martin/Nilles (Martin, 1987, 1978; Martin and Nilles, 1993). Since most of these researchers have focused on fixed beds of spherical pellets, our comparisons and analyses are thus conducted based on the heat transfer results in random packings of spheres with $N$ = 6.1. A comparison between the azimuthally-averaged temperature profile at cross section z = 9$d_p$ and the radial temperature profiles predicted by the 2D-ADPF model based on different correlations is shown in Fig. 14 for different $Re_p$. Overall, a detailed comparisons of radial temperature profiles demonstrates that the model of Specchia/Baldi/Gianetto/Sicardi (Specchia et al., 1980, 1978) for all flow regimes and of Martin/Nilles (Martin, 1987, 1978; Martin and Nilles, 1993) for the turbulent regime agree reasonably well with the CFD data for the cases investigated. It is worth remarking that the deviations observed for the other models, e.g. Yagi and Wakao (1959) and

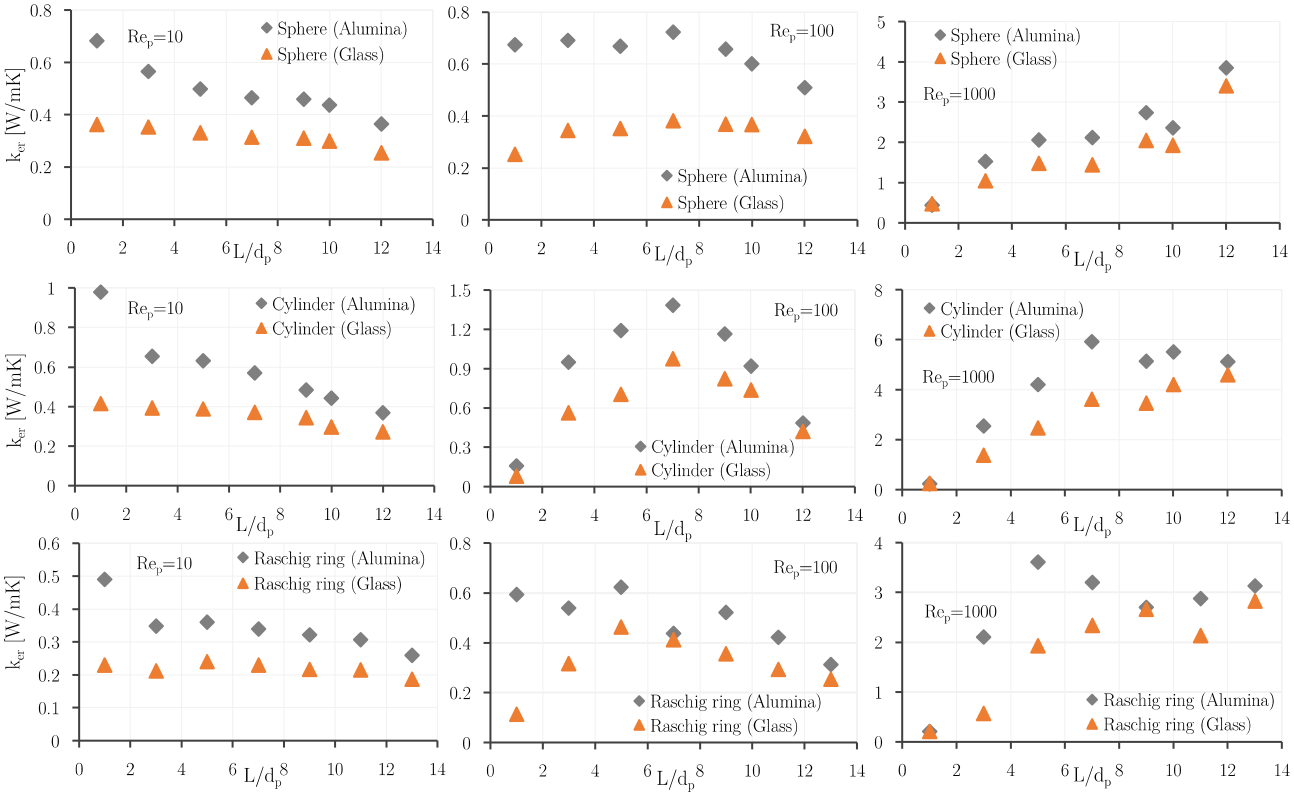


**Fig. 12.** Influence of pellet thermal conductivity and bed length on $k_{er}$ in random packing of spheres (first row), cylinders (second row) and Raschig rings (third row) with $N_{pv}$ = 3.1 at $Re_p$ = 10 (first column), 100 (second column) and 1000 (third column).

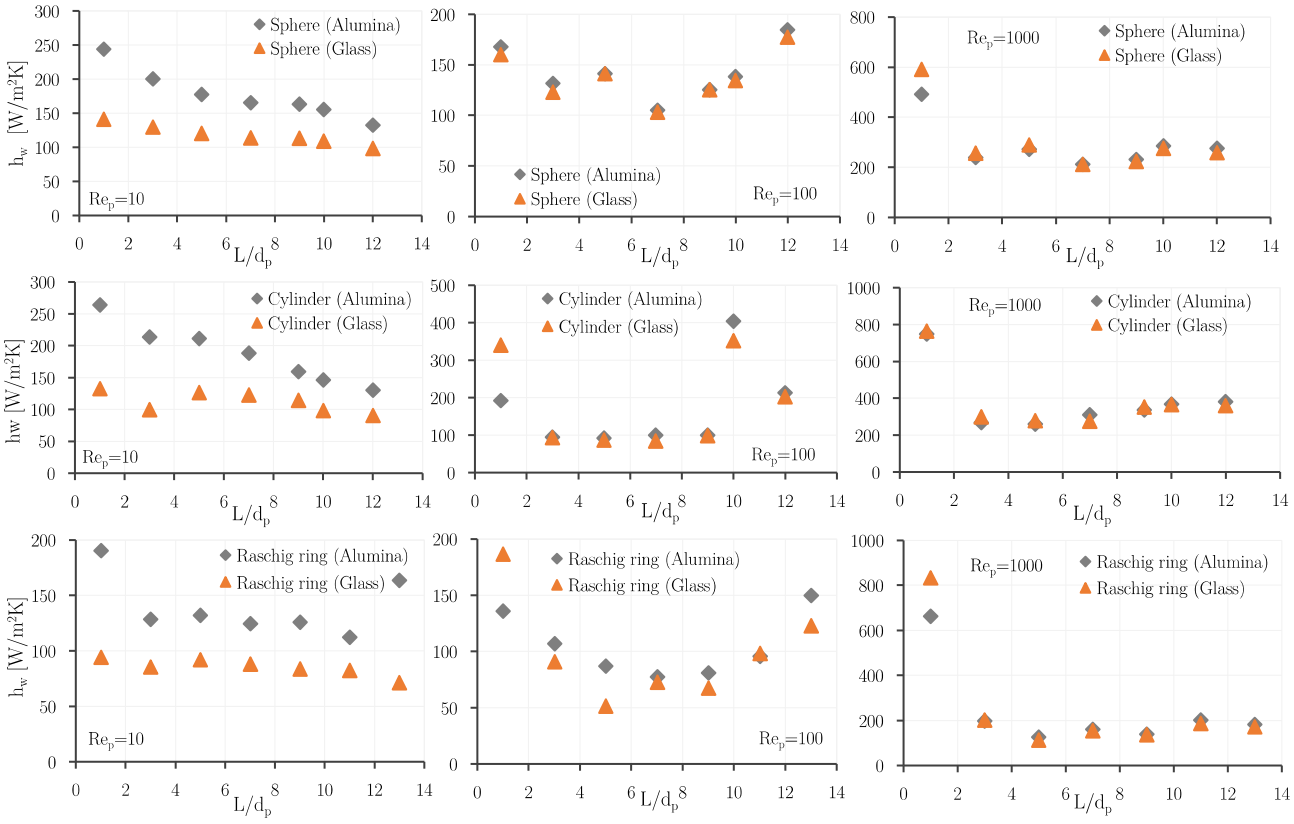


**Fig. 13.** Influence of pellet thermal conductivity and bed length on $h_w$ in random packing of spheres (first row), cylinders (second row) and Raschig rings (third row) with $N_{pv}$ = 3.1 at $Re_p$ = 10 (first column), 100 (second column) and 1000 (third column).

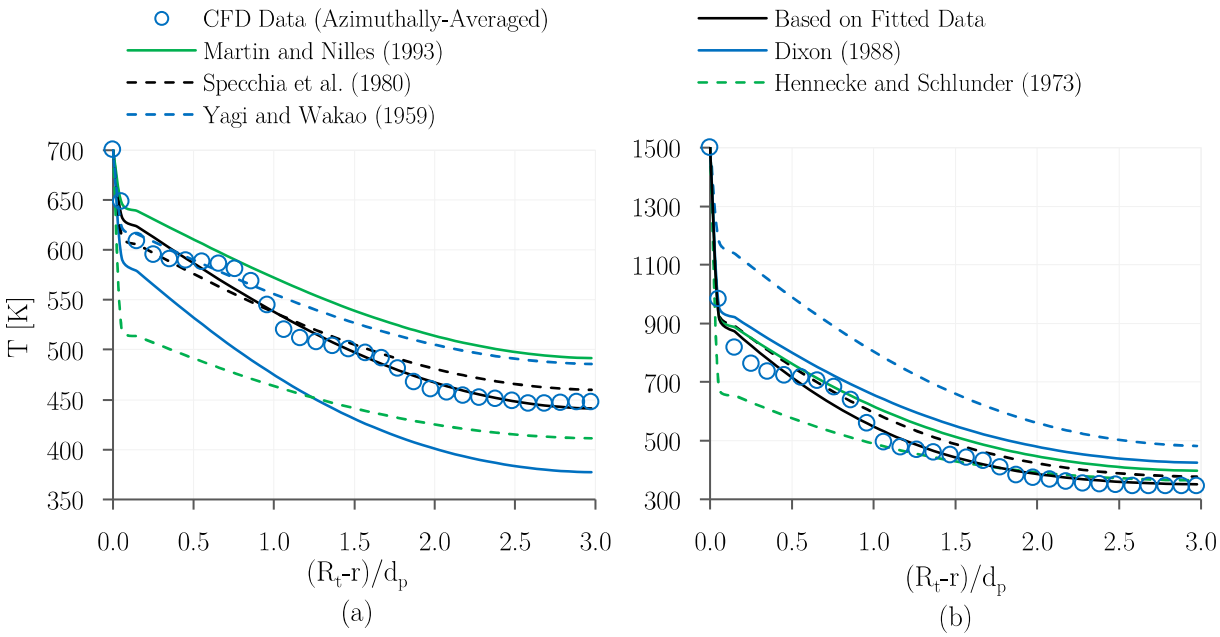


**Fig. 14.** Comparison between azimuthally-averaged temperature profile from detailed CFD simulations and the radial temperature profile predicted by 2D-ADPF model based on different correlations at the bed cross section z = $9d_p$ in random packing of spheres with N = 6.1; (a) $Re_p$ = 100 and (b) $Re_p$ = 1000.

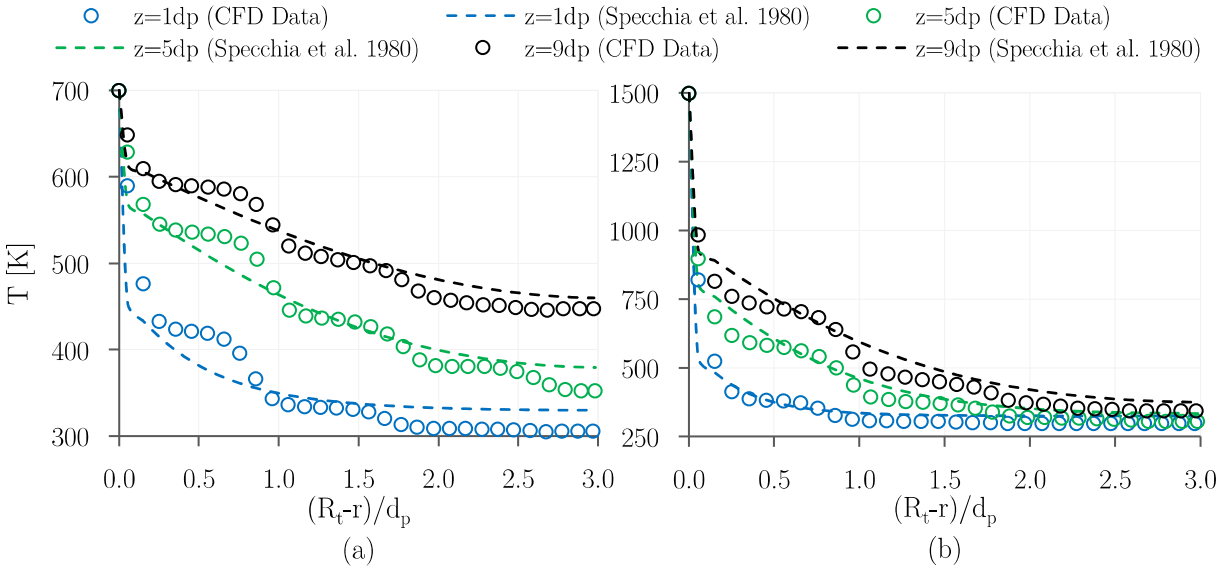


**Fig. 15.** Comparisons between azimuthally-averaged temperature profile from detailed CFD simulations and the radial temperature profile predicted by the model of Specchia et al. (1980) at different cross sections in random packing of spheres with N = 6.1; (a) $Re_p$ = 100 and (b) $Re_p$ = 1000.

Dixon (1988), in our typical case study, together with the inherent deviations which arise from the azimuthal-averaging of the 3D temperature field, can cause erroneous predictions of hotspot zones in tubular fixed bed reactors.

The accuracy of the model of Specchia/Baldi/Gianetto/Sicardi (Specchia et al., 1980, 1978) is further examined in Fig. 15 in terms of predicting the radial temperature profile at different axial positions along the bed. Results show a reasonable prediction of the radial temperature profile at different bed cross sections. However, it is evident that such a simplistic model cannot reproduce the trend of radial temperature distribution within a distance of one particle diameter from the wall, represented in the form of hump or shoulder shape, which, as explained before, is due to the presence of a high thermal disequilibrium between the two phases in this region.

## 5. Conclusion

Detailed numerical experiments of wall-to-bed heat transfer were conducted using fully-resolved discrete pellet CFD modelling, founded on sequential RBD and CFD simulations. The behavior of wall-to-bed heat transfer at different scales, from the detailed 3D pellet-scale to 2D radial temperature profiles, were investigated at different cross sections for packings of spheres, cylinders and Raschig rings. Overall, the results demonstrate a large deviation

of azimuthally-averaged temperature profiles from local temperature data, implicating the inadequacy of 2D-scale temperature profiles for predicting local heat transfer rates inside dense packing structures. Furthermore, the azimuthally averaged temperature profiles showed the presence of a hump or shoulder which usually occurs at an approximate distance of $0.8d_{pv}$ to $1d_{pv}$ from the tube wall in all packing models due to thermal disequilibrium between fluid and solid phases.

The effect of bed length on the volume-averaged effective heat transfer parameters used in the 2D-ADPF heat transfer model, i.e. $k_{er}$ and $h_w$, is thoroughly investigated by fitting the model predictions to the numerical results of heat transfer. Most previous research explained the length-dependence as caused by either the experimental error arising from poor/inadequate insulation of the calming section or the thermocouple's cross (e.g. Dixon, 1985, 2012; Dixon et al., 1988; Freiwald and Paterson, 1992, to name a few) or the under-developed velocity and thermal fields to be extended over a specific bed length after the bed entrance (Li and Finlayson 1971; Paterson and Carberry, 1983; Wen and Ding, 2006). This study, however, demonstrated that the length-dependence essentially originates from the evolutionary trend of thermal (non-)equilibrium between the fluid and solid phases along the bed.

A detailed sensitivity analysis was performed, whereby the influence of shape and thermal conductivity of catalyst pellets, as well as the tube-to-pellet diameter ratio, on both $k_{er}$ and $h_w$ were investigated. The results offer insight into the contribution of the different transport mechanisms on the effective thermal properties. The performance of the most promising theoretical- and empirical-based literature correlations for $Pe_{er}$ and $Nu_w$ were investigated in a comparison of the azimuthally-averaged temperature data obtained from discrete-pellet CFD simulation results. It is concluded that the models of Specchia/Baldi/Gianetto/ Sicardi (Specchia et al., 1980, 1978) for all flow regimes and of Martin/ Nilles (Martin, 1987, 1978; Martin and Nilles, 1993) for the turbulent regime can be recommended for practical use for spherical particle packings.

Overall, in spite of the severe shortcomings inherent in 2D pseudo-continuum models for predicting the thermal behavior of a fixed bed reactor such as: i) large deviations from local data, ii) a failure to anticipate the hump shape in the temperature profile, and iii) a length dependency of effective heat transfer parameters, this effort has shown that numerical experiments can be used as a design tool to tune such simplistic approaches to improve the reliability of the model results.

## CRediT authorship contribution statement

**E.M. Moghaddam:** Conceptualization, Methodology, Software, Investigation, Writing - original draft. **E.A. Foumeny:** Supervision. **A.I. Stankiewicz:** Supervision. **J.T. Padding:** Conceptualization, Supervision, Writing - review & editing.

## Declaration of Competing Interest

The authors declare that they have no known competing financial interests or personal relationships that could have appeared to influence the work reported in this paper.

## References


Bale, S., Sathe, M., Ayeni, O., Berrouk, A.S., Joshi, J., Nandakumar, K., 2017. Spatially resolved mass transfer coefficient for moderate Reynolds number flows in packed beds: wall effects. Int. J. Heat Mass Transf. 110, 406–415. https://doi.org/10.1016/j.ijheatmasstransfer.2017.03.052.

Bale, S., Tiwari, S., Sathe, M., Berrouk, A.S., Nandakumar, K., Joshi, J., 2018. Direct numerical simulation study of end effects and D / d ratio on mass transfer in packed beds. Int. J. Heat Mass Transf. 127, 234–244. https://doi.org/10.1016/j.ijheatmasstransfer.2018.07.100.

Bauer, R., Schlunder, E.U., 1978. Effective radial thermal-conductivity of packings in gas-flow. 2. Thermal-conductivity of packing fraction without gas-flow. Int. Chem. Eng. 18, 189–204.

Behnam, M., Dixon, A.G., Nijemeisland, M., Stitt, E.H., 2013. A new approach to fixed bed radial heat transfer modeling using velocity fields from computational fluid dynamics simulations. Ind. Eng. Chem. Res. 52, 15244–15261. https://doi.org/10.1021/ie4000568.

Bey, O., Eigenberger, G., 2001. Gas flow and heat transfer through catalyst filled tubes. Int. J. Therm. Sci. 40, 152–164. https://doi.org/10.1016/S1290-0729(00)01204-7.

Boccardo, G., Augier, F., Haroun, Y., Ferre, D., Marchisio, D.L., 2015. Validation of a novel open-source work-flow for the simulation of packed-bed reactors. Chem. Eng. J. 279, 809–820. https://doi.org/10.1016/j.cej.2015.05.032.

Borkink, J.G.H., Westerterp, K.R., 1994. Significance of the radial porosity profile for the description of heat transport in wall-cooled packed beds. Chem. Eng. Sci. 49, 863–876. https://doi.org/10.1016/0009-2509(94)80023-5.

Borkink, J.G.H., Westerterp, K.R., 1992. Determination of effective heta transport coefficients for wall-cooled packed beds. Chem. Eng. Sci. 47, 2337–2342.

Byrd, R.H., Gilbert, J.C., Nocedal, J., 2000. A trust region method based on interior point techniques for nonlinear programming. Math. Program. 89, 149–185.

Coleman, T.F., Li, Y., 1996. An interior trust region approach for nonlinear minimization subject to bounds. SIAM J. Optim. 6, 418–445.

Dai, X.P., Liu, P.Z., Shi, Y., Xu, J., Wei, W.S., 2014. Fischer-Tropsch synthesis in a bench-scale two-stage multitubular fixed-bed reactor: Simulation and enhancement in conversion and diesel selectivity. Chem. Eng. Sci. 105, 1–11.

de Wasch, A.P., Froment, G.F., 1972. Heat transfer in packed beds. Chem. Eng. Sci. 27, 567–576. https://doi.org/10.1016/0009-2509(72)87012-X.

Dixon, A.G., 1985. The length effect on packed bed effective heat transfer parameters. Chem. Eng. J. 31, 163–173.

Dixon, A.G., 1988. Wall and particle-shape effects on heat transfer in packed beds. Chem. Eng. Commun. 71, 217–237. https://doi.org/10.1080/00986448808940426.

Dixon, A.G., 1996. An improved equation for the overall heat transfer coefficient in packed beds. Chem. Eng. Process. Process Intensif. 35, 323–331.

Dixon, A.G., 2012. Fixed bed catalytic reactor modelling—the radial heat transfer problem. Can. J. Chem. Eng. 90, 507–527.

Dixon, A., Cresswell, D.L., Paterson, W.R., 1978. Heat Transfer in Packed Beds of Low Tube to Particle Diameter Ratio, ACS Symp. Ser. No. 65, 238. Edinburgh.

Dixon, A., Cresswell, D., 1979. Theoretical prediction of effective heat transfer parameters in packed beds. AIChE J. 25, 663–676. https://doi.org/10.1002/aic.690250413.

Dixon, A.G., Cresswell, D.L., 1986. Effective heat transfer parameters for transient packed-bed models. AIChE J. 32, 809–819. https://doi.org/10.1002/aic.690320511.

Dixon, A.G., van Dongeren, J.H., 1998. The influence of the tube and particle diameters at constant ratio on heat transfer in packed beds 1. Chem. Eng. Process. Process Intensif. 37, 23–32.

Dixon, A.G., Nijemeisland, M., Stitt, E.H., 2006. Packed tubular reactor modeling and catalyst design using computational fluid dynamics. Adv. Chem. Eng. 31, 307–389. https://doi.org/10.1016/S0065-2377(06)31005-8.

Dixon, A.G., Tsotsas, E., Martin, H., 1988. Letters to the editor- thermal conductivity of packed beds. Chem. Eng. Process. Process Intensif. 24, 177–179.

Dixon, A.G., Walls, G., Stanness, H., Nijemeisland, M., Stitt, E.H., 2012. Experimental validation of high Reynolds number CFD simulations of heat transfer in a pilot-scale fixed bed tube. Chem. Eng. J. 200–202, 344–356. https://doi.org/10.1016/j.cej.2012.06.065.

Dong, Y., Sosna, B., Korup, O., Rosowski, F., Horn, R., Sosna, B., Korup, O., Rosowski, F., Horn, R., 2017. Investigation of radial heat transfer in a fixed-bed reactor: CFD simulations and profile measurements. Chem. Eng. J. 317, 204–214. https://doi.org/10.1016/j.cej.2017.02.063.

Eppinger, T., Seidler, K., Kraume, M., 2011. DEM-CFD simulations of fixed bed reactors with small tube to particle diameter ratios. Chem. Eng. J. 166, 324–331. https://doi.org/10.1016/j.cej.2010.10.053.

Finlayson, B.A., 1971. Packed bed reactor analysis by orthogonal collocation. Chem. Eng. Sci. 26, 1081–1091.

Flaischlen, S., Wehinger, G.D., 2019. Synthetic packed-bed generation for CFD simulations: blender vs. STAR-CCM+. ChemEngineering 3, 52. https://doi.org/10.3390/chemengineering3020052.

Freiwald, M.G., Paterson, W.R., 1992. Accuracy of model predictions and reliability of experimental data for heat transfer in packed beds. Chem. Eng. Sci. 47, 1545–1560. https://doi.org/10.1016/0009-2509(92)85003-T.

Freund, H., Bauer, J., Zeiser, T., Emig, G., 2005. Detailed simulation of transport processes in fixed-beds. Ind. Eng. Chem. Res. 44, 6423–6434. https://doi.org/10.1021/ie0489453.

Freund, H., Zeiser, T., Huber, F., Klemm, E., Brenner, G., Durst, F., Emig, G., 2003. Numerical simulations of single phase reacting flows in randomly packed fixed-bed reactors and experimental validation. Chem. Eng. Sci. 58, 903–910. https://doi.org/10.1016/S0009-2509(02)00622-X.

Gunn, D.J., Khalid, M., 1975. Thermal dispersion and wall effect in packed beds. Chem. Eng. Sci. 30, 261–267.

Guo, Z., Sun, Z., Zhang, N., Ding, M., Zhou, Y., 2019. Influence of flow guiding conduit on pressure drop and convective heat transfer in packed beds. Int. J. Heat Mass Transf. 134, 489–502. https://doi.org/10.1016/j.ijheatmasstransfer.2019.01.066.

Hennecke, F.-W., Schlünder, E.U., 1973. Wärmeübergang in beheizten oder gekühlten Rohren mit Schüttungen aus Kugeln. Zylindern und Raschig-Ringen. Chemie Ing. Tech. 45, 277–284. https://doi.org/10.1002/cite.330450510.
Jurtz, N., Kraume, M., Wehinger, G.D., 2019. Advances in fixed-bed reactor modeling using particle-resolved computational fluid dynamics (CFD). Rev. Chem. Eng. 35, 139–190. https://doi.org/10.1515/revce-2017-0059.
Li, Chi-Hsiung, Finlyson, B.A., 1976. Heat transfer in packed beds - a reevaluation. Chem. Eng. Trans. 32, 1055–1066.
Magnico, P., 2009. Pore-scale simulations of unsteady flow and heat transfer in tubular fixed beds. AIChE J. 55, 849–866. https://doi.org/10.1002/aic.11806.
Martin, H., 1978. Low Peclet number particle-to-fluid heat and mass transfer in packed beds. Chem. Eng. Sci. 33, 913–919.
Martin, H., 1987. Thermal conductivity of packed beds: a review. Chem. Eng. Process: Process Intensif. 22 (1), 19–37.
Martin, H., Nilles, M., 1993. Radiale Warmeleitung in durchstromten Schuttungsrohren. Chem. Ing. Tech. 65, 1468–1477.
Melanson, M.M., Dixon, A.G., 1985. Solid conduction in low dt/dp beds of spheres, pellets and rings. Int. J. Heat Mass Transf. 28, 383–394. https://doi.org/10.1016/0017-9310(85)90071-7.
Moghaddam, E.M., Foumeny, E.A., Stankiewicz, A.I., Padding, J.T., 2018. Rigid body dynamics algorithm for modeling random packing structures of nonspherical and nonconvex pellets. Ind. Eng. Chem. Res. 57, 14988–15007. https://doi.org/10.1021/acs.iecr.8b03915.
Moghaddam, E.M., Foumeny, E.A., Stankiewicz, A.I., Padding, J.T., 2019. Fixed bed reactors of non-spherical pellets: importance of heterogeneities and inadequacy of azimuthal averaging. Chem. Eng. Sci. X 1,. https://doi.org/10.1016/j.cesx.2019.100006 100006.
Moghaddam, E.M., Foumeny, E.A., Stankiewicz, A.I., Padding, J.T., 2020. Hydrodynamics of narrow-tube fixed bed reactors filled with Raschig rings. Chem. Eng. Sci. X 5,. https://doi.org/10.1016/j.cesx.2020.100057 100057.
Moghaddam, E.M., Foumeny, E.A., Stankiewicz, A.I., Padding, J.T., 2021. Heat transfer from wall to dense packing structures of spheres, cylinders and Raschig rings. Chem. Eng. J. 407,. https://doi.org/10.1016/j.cej.2020.127994 127994.
Nekhamkina, O., Sheintuch, M., 2009. Approximate characteristics of a moving temperature front in a fixed-bed catalytic reactor: effect of mass dispersion. Chem. Eng. J. 154, 115–119. https://doi.org/10.1016/j.cej.2009.04.043.
Nijemeisland, M., Dixon, A.G., 2001. Comparison of CFD simulations to experiment for convective heat transfer in a gas-solid fixed bed. Chem. Eng. J. 82, 231–246. https://doi.org/10.1016/S1385-8947(00)00360-0.
Obalová, L., Jirátová, K., Karásková, K., Chromčáková, Ž., 2012. N2O catalytic decomposition–From laboratory experiment to industry reactor. Catal. Today 191, 116–120.
Partopour, B., Dixon, A.G., 2019. 110th Anniversary: commentary: CFD as a modeling tool for fixed bed reactors. Ind. Eng. Chem. Res. 58, 5733–5736. https://doi.org/10.1021/acs.iecr.8b06380.
Partopour, B., Dixon, A.G., 2017. Resolved-particle fixed bed CFD with microkinetics for ethylene oxidation. AIChE J. 63, 87–94. https://doi.org/10.1002/aic.15422.
Paterson, W.R., Carberry, J.J., 1983. Fixed bed catalytic reactor modelling: the heat transfer problem. Chem. Eng. Sci. 38, 175–180. https://doi.org/10.1016/0009-2509(83)80149-3.
Romkes, S.J., Dautzenberg, F., van den Bleek, C., Calis, H.P., 2003. CFD modelling and experimental validation of particle-to-fluid mass and heat transfer in a packed bed at very low channel to particle diameter ratio. Chem. Eng. J. 96, 3–13. https://doi.org/10.1016/j.cej.2003.08.026.
Ruiz, G., Ripoll, N., Fedorova, N., Zbogar-Rasic, A., Jovicic, V., Delgado, A., Toledo, M., 2019. Experimental and numerical analysis of the heat transfer in a packed bed exposed to the high thermal radiation flux. Int. J. Heat Mass Transf. 136, 383–392. https://doi.org/10.1016/j.ijheatmasstransfer.2019.03.009.
Schlereth, D., Hinrichsen, O., 2014. A fixed-bed reactor modeling study on the methanation of CO2. Chem. Eng. Res. Des. 92, 702–712.
Singhal, A., Cloete, S., Radl, S., Quinta-Ferreira, R., Amini, S., 2017a. Heat transfer to a gas from densely packed beds of monodisperse spherical particles. Chem. Eng. J. 314, 27–37. https://doi.org/10.1016/j.cej.2016.12.124.
Singhal, A., Cloete, S., Radl, S., Quinta-Ferreira, R., Amini, S., 2017b. Heat transfer to a gas from densely packed beds of cylindrical particles. Chem. Eng. Sci. 172, 1–12. https://doi.org/10.1016/j.ces.2017.06.003.
Specchia, V., Baldi, G., Gianetto, A., 1978. Solid-liquid mass transfer in concurrent two-phase flow through packed beds. Ind. Eng. Chem. Process Des. Dev. 17, 362–367.
Specchia, V., Baldi, G., Sicardi, S., 1980. Heat transfer in packed bed reactors with one phase flow. Chem. Eng. Commun. 4, 361–380. https://doi.org/10.1080/00986448008935916.
Taskin, M.E., Dixon, A.G., Nijemeisland, M., Stitt, E.H., 2008. CFD Study of the influence of catalyst particle design on steam reforming reaction heat effects in narrow packed tubes. Ind. Eng. Chem. Res. 47, 5966–5975. https://doi.org/0.1021/ie800315d.
Vortmeyer, D., Haidegger, E., 1991. Discrimination of three approaches to evaluate heat fluxes for wall-cooled fixed bed chemical reactors. Chem. Eng. Sci. 46, 2651–2660. https://doi.org/10.1016/0009-2509(91)80058-7.
Wakao, N., Kaguei, S., Funazkri, T., 1979. Effect of fluid dispersion coefficients on particle-to-fluid heat transfer coefficients in packed beds: correlation of Nusselt numbers. Chem. Eng. Sci. 34, 325–336.
Wakao, N., Kaguei, S., Nagai, H., 1978. Effective diffusion coefficients for fluid species reacting with first order kinetics in packed bed reactors and discussion on evaluation of catalyst effectiveness factors. Chem. Eng. Sci. 33, 183–187.
Waltz, R.A., Morales, J.L., Nocedal, J., Orban, D., 2006. An interior algorithm for nonlinear optimization that combines line search and trust region steps. Math. Program. 107, 391–408.
Wehinger, G.D., Fu, C., Kraume, M., 2017. Contact modifications for CFD simulations of fixed-bed reactors: cylindrical particles. Ind. Eng. Chem. Res 56 (1), 87–99. https://doi.org/10.1021/acs.iecr.6b03596.
Wen, D., Ding, Y., 2006. Heat transfer of gas flow through a packed bed. Chem. Eng. Sci. 61, 3532–3542. https://doi.org/10.1016/j.ces.2005.12.027.
Yagi, S., Kund, D., 1964. Heat transfer in packed beds through which water is flowing. Int. J. Heat Mass Transf. 7, 333–339.
Yagi, S., Kunii, D., 1957. Studies on effective thermal conductivities in packed beds. AIChE J. 3, 373–381. https://doi.org/10.1002/aic.690030317.
Yagi, S., Wakao, N., 1959. Heat and mass transfer from wall to fluid in packed beds. AIChE J. 5, 79–85.
Zehner, P., Schlünder, E.U., 1970. Wärmeleitfähigkeit von Schüttungen bei mäßigen Temperaturen. Chem. Ing. Tech. 42, 933–941.
Zehner, P., Schlünder, E.U., 1973. Die effektive Wärmeleitfähigkeit durchströmter Kugelschüttungen bei mäßigen und hohen Temperaturen. Chem. Ing. Tech. 45, 272–276.

## Further reading

H.Borkink, J.G., Westerterp, K.R., 1992. Influence of tube and aprticle diameter on heat transport in packed beds. AIChE J. 38, 703–716.